The GALAH survey and *Gaia* DR2: forced oscillation and phase mixing in the local stellar disc

Joss Bland-Hawthorn[1,2,3][⋆], Sanjib Sharma[1,2], Thor Tepper-Garcia[1], James Binney[4], Ken C. Freeman[5], Michael R. Hayden[1,2], Janez Kos[1], Gayandhi M. De Silva[1,6], Geraint F. Lewis[1], Martin Asplund[2,5], Sven Buder[7,8], Andrew R. Casey[9,10], Valentina D'Orazi[11], Ly Duong[5], Prajwal R. Kafle[12], Jane Lin[5], Karin Lind[13], Sarah L. Martell[14], Melissa K. Ness[15,16], Jeffrey D. Simpson[13], Daniel B. Zucker[6], Tomaž Zwitter[17] and the GALAH team

(Affiliations listed after the references)

16 August 2018

ABSTRACT

We use data from the second data releases of the ESA *Gaia* astrometric survey and the high-resolution GALAH spectroscopic survey to analyse the structure of our Galaxy's discs. With GALAH, we can separate the α-rich and α-poor discs (with respect to Fe), which are superposed in both position and velocity space, and examine their distributions in action space. We examine carefully the distribution of stars in the zV_z phase plane in which a remarkable "phase spiral" was recently discovered. We show that the spiral extends well beyond the narrow cylinder in which it was found and is present in both discs but appears most clearly in stars on less eccentric orbits. We display the phase spiral in V_ϕ in addition to V_R and identify the signature in the zV_z plane of a tilting velocity ellipsoid. The spiral is presumably a signature of a non-equilibrium stellar distribution phase mixing, but our results rule out the idea that it is associated with disrupting star clusters. We present new simulations of tidal disturbance of the Galactic disc by a halo substructure similar to the Sgr dwarf. The effects on the zV_z plane of the substructure passing through the disc last at least $2\,\mathrm{Gyr}$, but a subsequent disc crossing wipes out the coherent structure. These simulations suggest that the phase spiral was created $\sim 0.5\,\mathrm{Gyr}$ ago as an object like Sgr with total mass $\sim 3 \times 10^{10}\mathrm{M}_\odot$ (stripped down from $\sim 5 \times 10^{10}\mathrm{M}_\odot$ when it first entered the halo) passed through the plane.

Key words: Surveys – the Galaxy – stars: abundances – stars: dynamics – stars: kinematics

]

1 INTRODUCTION

The ESA *Gaia* astrometric mission (Perryman et al. 2001; Prusti et al. 2016) has been eagerly anticipated for many years by the stellar and Galactic communities and the early results have not disappointed (DR2: Brown et al. 2018). Wide-field stellar surveys across the Galaxy are fundamental to astrophysics because there are important measurements that can only be made in the near field. The remarkable precision of measured stellar parameters by *Gaia* after only two years of observations has triggered a flurry of new discoveries and new fields of study (e.g. Antoja et al. 2018; Eyer et al. 2018; Marchetti et al. 2018; Koppelman et al. 2018; Malhan et al. 2018). Complementary spectroscopic surveys (RAVE, APOGEE, LAMOST, *Gaia* -ESO) and are now able to exploit the overlap of targets with *Gaia* DR2 – this is the golden age of Galactic archaeology (Freeman & Bland-Hawthorn 2002).

Our focus here is on the synergy between *Gaia* and

⋆ Contact e-mail: jbh@physics.usyd.edu.au

the Galactic Archaeology with HERMES (GALAH)[1] survey based at the Anglo-Australian Telescope (AAT) in Australia. This survey brings a unique perspective to Galactic archaeology by measuring accurate radial velocities and up to 30 elemental abundances (more for the brightest stars) for about a million stars (De Silva et al. 2015; Martell et al. 2017). The HERMES instrument was designed and optimised for the GALAH survey specifically for the pursuit of Galactic archaeology (Freeman & Bland-Hawthorn 2008; Barden et al. 2010). The GALAH selection criteria were designed to be as simple as possible to avoid problems that adversely affect earlier surveys (Sharma et al. 2011). The primary selection is based on a magnitude range of $12 < V < 14$ and a cut in Galactic latitude, $|b| > 10 \deg$. Thus GALAH probes mainly the thin and thick discs of the Galaxy. The impact of *Gaia* was a key consideration from the outset, particularly with regard to choosing a bright limiting magnitude to ensure good distances for all stars.

The second GALAH data release (GALAH DR2) features stellar parameters, radial velocities and up to 23 elemental abundances for $342\,682$ stars (Buder et al. 2018). All of these stars have complementary data from the *Gaia* DR2 data archive. GALAH's high-quality radial velocities, with mean errors of $0.1-0.2$ km s^{-1} (Zwitter et al. 2018), are much better than the *Gaia* radial velocities, but comparable to or better than typical transverse velocities derived from the proper motions (Brown et al. 2018). The GALAH-*Gaia* synergy[2] is particularly strong for local dwarfs that dominate the survey within about 1 kpc. We exploit this advantage in the present study.

A major topic is the remarkable discovery of a phase-space signal in the local stellar disc by the *Gaia* team (Antoja et al. 2018). In a volume element defined by $(\Delta R, \Delta \phi, \Delta z) = (\pm 0.1, \pm 0.1, \pm 1)$ kpc^3 centred on the Sun, Antoja et al. (2018) detect a coherent spiral pattern in the space spanned by z and V_z. This phenomenon is indicative of a system that is relaxing from a mildly disturbed state to a stationary configuration (Lynden-Bell 1967) through the process of phase mixing (e.g. Binney & Tremaine 2008, §4.10.2).

In Section 2 we establish notation and define the required coordinate systems. In Section 3 we characterise the GALAH survey and use it to understand better the gross structure of the Galaxy's discs. In Section 4 we analyse the phase spiral in detail using data from *Gaia*, Galah and LAMOST and taking advantage of the insights provided by angle-action coordinates. In Section 5 we present a novel manifestation of the tilt of the velocity ellipsoid as one moves away from the plane, and discuss the relation of the spirals seen in V_R and V_ϕ. In Section 6, some dynamical implications are considered prior to a search, in Section 7, for the phase spiral signal in N-body simulations of Sgr impacting the Galactic disc. Section 8 sums up and provides some pointers to future work.

---

2   COORDINATES

2.1   Terminology

Since the seminal work of Gilmore & Reid (1983) we have become accustomed to the idea that the Galaxy's disc comprises two components. Traditionally these have been called the thin and the thick discs because Gilmore & Reid (1983) distinguished them by their contrasting vertical density profiles. In the last few years, it has become clear that this terminology is unfortunate because the real dichotomy is between stars that are poor and rich in α elements (e.g. O, Ne, Mg, Si) with respect to iron.

Chemistry always provides a firmer foundation for galaxy dissection than kinematics or spatial distribution because a star's chemical composition is invariant even as its orbit evolves, and thus its kinematics and spatial distributions evolve. Moreover, the classical thin and thick discs were always understood to overlap extensively in both real and velocity space, so in much of phase space stars cannot be assigned to one disc or the other if only phase-space coordinates are known. Hence dissection by chemistry is always the preferred option.

As the numbers of stars with good spectra has grown, it has become clear that α-rich stars form a structure that is quite different from that formed by α-poor stars. Figure 1 summarises our current understanding of the Galaxy's discs. A disc comprising α-rich stars extends out to about the solar radius, having a scaleheight of order 1 kpc. A disc comprising α-poor stars extends beyond the solar radius. Out to that radius it has a scaleheight of order 0.3 kpc but further out it flares, so at large radii α-poor stars can be found far from the plane.

In view of this picture, we shall refer to the α-poor and α-rich discs rather than to the thin and thick discs.

2.2   Reference frame

We employ righthanded frames of reference for both the heliocentric and Galactocentric systems. In the heliocentric system, the x axis and unit vector $\mathbf{i}$ point towards the Galactic Centre, the y axis and unit vector $\mathbf{j}$ point in the direction of rotation, and the z axis and unit vector $\mathbf{k}$ point towards the North Galactic Pole (NGP). Hence we place Sgr A* at $(x, y, z) = (R_0, 0, -z_0)$ kpc, where $R_0 = 8.2 \pm 0.1$ kpc and $z_0 = 25 \pm 5$ pc (Bland-Hawthorn & Gerhard 2016) consistent with the new ESO Gravity measurement (Gravity Collaboration et al. 2018), and the Sun's velocity with respect to a co-located particle on a circular orbit is $\mathbf{v}_{\rm LSR} = U_\odot \mathbf{i} + V_\odot \mathbf{j} + W_\odot \mathbf{k}$, with $(U_\odot, V_\odot, W_\odot) = (11, 10, 7.25)$ km s^{-1} (Schönrich 2012).

We employ Galactocentric cylindrical coordinates (R, ϕ, z) centred on Sgr A* with ϕ increasing clockwise when viewed from the north and the Sun located at $\phi_0 = \pi$. To convert velocities from the heliocentric to the Galactocentric frame, we take the angular velocity of the Sun to be $\Omega_\odot = (\Theta_0 + V_\odot)/R_0 = 30.24$ km s^{-1} kpc^{-1} from the measure proper motion of Sgr A* (Reid & Brunthaler 2004). The circular speed at the Sun is then $\Theta_0 = 238$ km s^{-1} (Bland-Hawthorn & Gerhard 2016). We ignore any correction to $\mathbf{v}_{\rm LSR}$ for streaming motions with respect to the LSR (e.g. Sharma et al. 2014; Gravity Collaboration et al. 2018).
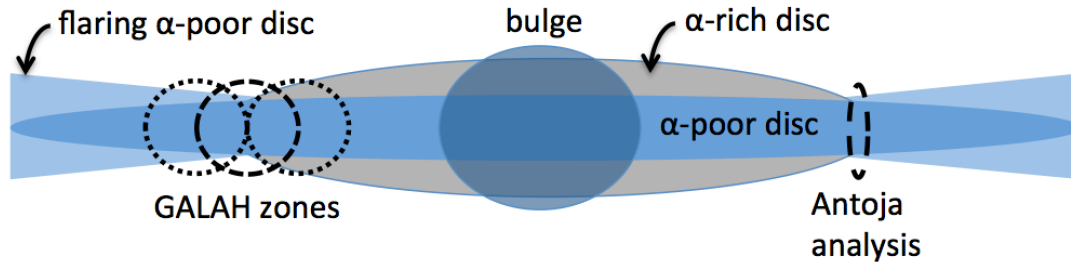
Figure 1. Schematic diagram of the modern interpretation of the disc structure (e.g. Hayden et al. 2015). The α-rich, inner thick disc has a shorter scalelength than the α-poor inner thin disc and terminates near the Solar Circle. Here, the α-poor disc takes over and begins to flare at larger radius. It is appropriate now to speak of the α-rich and α-poor discs (relative to Fe) rather than the thick and thin discs. The thin vertical ellipse shows the extent of the Antoja et al. (2018) *Gaia* analysis; the large dashed and dotted circles show the domain of our analysis. Both studies were performed in the solar neighbourhood. The stellar metallicity [Fe/H] declines with both R and z increasing everywhere across the Galaxy.

2.3 Angle-action variables

Motion in the zV_z plane is simplest when cast in terms of angle-action coordinates (Binney & Tremaine 2008; Binney & Schönrich 2018). The actions J_r and J_z quantify the amplitudes of a star's oscillation parallel and perpendicular to the Galactic plane, respectively. In an axisymmetric potential, the third action J_ϕ is the component of angular momentum around the symmetry axis: $J_\phi \equiv L_z$. Each action J_i is associated with an angle variable θ_i such that $(\boldsymbol{\theta}, \mathbf{J})$ forms a complete set of canonical coordinates for phase space. In the potential for which they are defined, the actions are constants of motion, while the angle variables increase linearly in time $\theta_i(t) = \theta_i(0) + \Omega_i t$, where the Ω_i are the star's three fundamental frequencies. We use the software package `AGAMA` (Vasiliev 2018) to compute angles and actions for motion in the Galactic potential derived by McMillan (2017). We quote actions with dimensions $L^2 T^{-1}$ as multiples of $R_0 \Theta_0 = 1952 \, \text{kpc}^2 \, \text{km s}^{-1}$.

3 DISC DISSECTION WITH GALAH DATA

The GALAH survey exploits the High Efficiency and Resolution Multi-Element Spectrograph (HERMES) at the Anglo-Australian Telescope (Sheinis et al. 2015). This instrument employs the Two Degree Field (2dF) fibre positioner at the f/3.3 Prime Focus to provide multi-object ($n \approx 400$), high-resolution ($\mathcal{R} \approx 28,000$) spectra of many stars in a single shot. HERMES is a fibre-fed, multi-channel spectrograph optimised to carry out Galactic archaeology from a 4m-class telescope (De Silva et al. 2015). HERMES has four optical spectrographs covering 471–490 nm, 564–587 nm, 647–673 nm and 758–788 nm for determining elemental abundances for up to 30 elements (up to 45 elements for the brightest stars). HERMES exploits a photonic comb to internally calibrate the fibre to fibre response across the full field of all four detectors(Bland-Hawthorn et al. 2017; Kos et al. 2018b).

Here we use the internal data release of 505 571 stars provided to the GALAH team which includes GALAH DR2 (Buder et al. 2018) augmented with HERMES data from parallel observations of open clusters, and K2 (Wittenmyer et al. 2018) and TESS fields (Sharma et al. 2018). These new
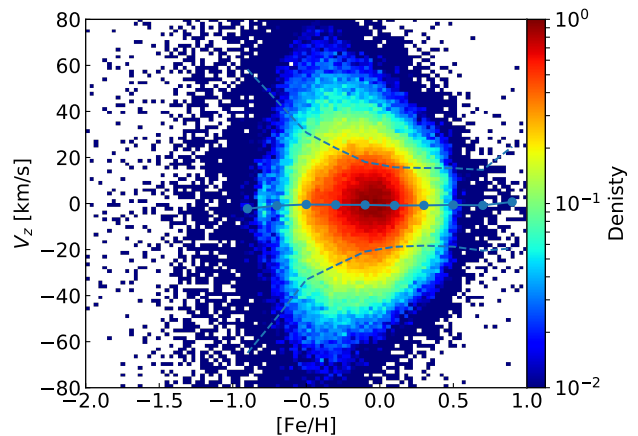

Figure 2. The trend in [Fe/H] vs. V_z colour coded in terms of relative density per pixel. This is mostly understood in terms of the well known age-metallicity and age-velocity dispersion relations (e.g. Sharma et al. 2014). [Fe/H] is taken from the GALAH survey; V_z is determined from *Gaia* proper motions and GALAH radial velocities. The mean trend is indicated; the 1σ error tracks show the progression from the thin disc to the thick disc and halo as [Fe/H] declines. This is important for understanding the visibility of the phase spiral in different metallicity bins.

observations, which provide improved calibrations of stellar masses and gravities, were reduced with the same pipeline as DR2 (Kos et al. 2017). The additional numbers of stars are 2 498, 97 133 and 42 764, respectively. From this sample, we select stars with the *Gaia* DR2 relative parallax uncertainty of less than 20% and distance $|R - R_0| \leqslant 1.0$ and $|\phi - \phi_0| \leqslant 15°$. These criteria yield a sample of 192 972 stars.

3.1 Chemodynamic correlations

Figure 2 shows the density of GALAH stars in the plane of [Fe/H] and V_z. The Sun lies near the density peak around (0,0). As [Fe/H] becomes negative, the density decreases at first gradually and then at [Fe/H] ~ -0.7 very steeply as the α-rich disc gives way to the halo. At positive [Fe/H], the
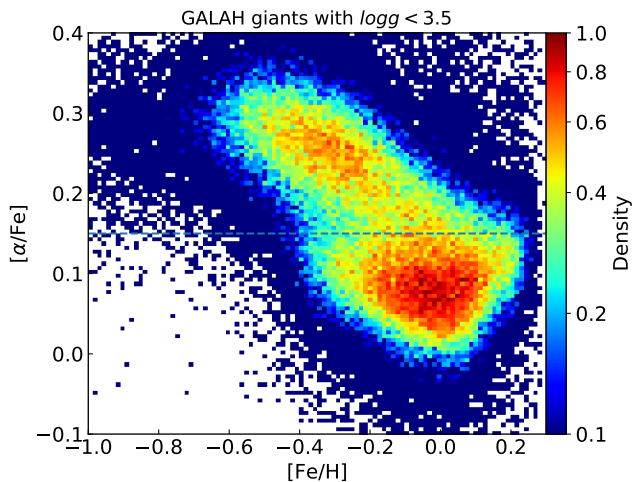
Figure 3. Distribution of giants in the [Fe/H] vs. [α/Fe] plane using data from the GALAH survey. Giants were selected with $\log g$ < 3.5. A clear separation of the high and low [α/Fe] populations is visible. The dashed boundary line distinguishes the high and low [α/Fe] populations (cf. Adibekyan et al. 2012). The simple choice of boundary is vindicated in Section 4.3 where we show that the dynamical properties (actions) of the high and low [α/Fe] populations are distinct.

falloff in density becomes steep at [Fe/H] $\sim$ 0.4, significantly more metal-rich than the metallicity of the local ISM. This is the signature of radial migration (Sellwood & Binney 2002; Schönrich & Binney 2009).

The dashed lines in Figure 2 show the standard deviation in V_z at a given [Fe/H]. This is remarkably flat at $\sim$ 20 km s^{-1} for [Fe/H] > -0.1, but as [Fe/H] falls below -1, it increases with ever-increasing rapidity. The increase of σ_z as [Fe/H] decreases reflects (a) stochastic acceleration of stars (Aumer et al. 2016) causes older, more metal-poor, populations within the thin disc to have larger velocity dispersions, and (b) as [Fe/H] drops the α-rich disc becomes more important, and its stars have large σ_z (hence its thickness).

Figure 3 shows the distribution in the ([Fe/H], [α/Fe]) plane of GALAH stars that are classified as giants ($\log g$ < 3.5). The distribution is strongly bimodal. We use the horizontal dashed line to classify stars as members of either the α-rich or α-poor disc. This is a simpler definition than one used in many other studies, which divide the discs by a line that runs down toward [α/Fe] $\sim$ 0 at the largest values of [Fe/H]. No convincing argument supported by data has been presented for the more complicated separation. We adopt the horizontal line in Figure 3 because it reflects the bimodality that is unambiguously present in Figure 3 and because GALAH captures significantly fewer α-rich stars than α-poor ones, so it is better to contaminate the α-poor sample with a few α-rich stars than allow significant contamination of the α-rich sample by outliers from the α-poor disc.

Figure 4 contrasts the action distributions of stars of different chemical compositions. From top to bottom, the panels of the left column (a), (d) and (g) show the distributions over J_r, J_z and L_z for all stars. The middle and right columns separate them into α-rich and α-poor stars, respec-

tively. Panel (h) shows that, in the α-rich disc, L_z tends to grow with [Fe/H] while panel (i) shows that the opposite correlation prevails in the α-poor disc. The decrease of [Fe/H] with increasing L_z in the α-poor disc reflects the radial metallicity gradient that is a general feature of galaxies. This gradient is fairly well understood (Schönrich & Binney 2009). That the α-rich disc shows the opposite correlation was discovered by Spagna et al. (2010), but is not well understood.

Comparison of panels (b) and (e) reveal that, in the α-rich disc, the distributions of J_r and J_z are remarkably similar. By contrast, panels (c) and (f) show that in the α-poor disc, the distribution in J_z is much narrower than the distribution of J_r. Given that J_r controls the in-plane dispersions σ_R and σ_ϕ, these contrasting action distributions imply that, whereas the α-rich disc has[3] σ_R < σ_z, in the α-poor disc, we find $\sigma_R \sim 2.5\sigma_z$. The origin of the anisotropy of the α-poor disc has long been understood to arise from the tendency of spiral arms to heat the disc only within the plane while random motion in the vertical direction requires scattering by molecular clouds (Jenkins & Binney 1990; Ida et al. 1993; Aumer et al. 2016). The contrasting anisotropy of the α-rich disc was inferred by Binney (2012) when fitting distribution functions that depend on actions to data from the Geneva-Copenhagen survey (Nordström et al. 2004; Holmberg et al. 2009). Its physical cause, however, remains obscure. Note that at metallicities [Fe/H] < -1 characteristic of the halo, the popular values of J_z do not increase in line with the popular values of J_r. Thus the halo, like the α-poor disc, favours J_r over J_z and has σ_R > σ_z; *the α-rich disc is unique in its preference for J_z.*

In Figure 4(f), the J_r distribution of the α-poor stars has a much sharper top-right corner than the corresponding distribution of J_z shown in panel (c). This indicates that the most metal-rich stars extend to the largest values of J_r but they shun the largest values of J_z. This phenomenon has two possible explanations. One is that spiral structure almost instantaneously accelerates stars to significant random velocities within the plane but it takes significant time for molecular clouds to convert in-plane motion to vertical motion (Aumer et al. 2016). The other possible explanation is that the most metal-rich stars can enter the GALAH sample only by migrating outwards from their birth radii, and stars with large J_z are less likely to migrate than stars with small J_z (Solway et al. 2012). It is interesting to note that the upper envelopes of the J_r and J_z distributions of the α-rich stars are almost identical with the most metal-rich stars shunning the highest values of both actions.

---

[3] The following argument explains why equal widths in J_r and J_z imply σ_R < σ_z rather than $\sigma_R \simeq \sigma_z$:

$$2\pi J_i = \oint \dot{x}_i \, dx_i = \frac{1}{\Omega_i} \int_0^{2\pi} (\dot{x})^2 \, d\theta_i = \frac{2\pi}{\Omega_i} \langle v_i^2 \rangle. \qquad (1)$$

So the time-average of a star's squared velocity component, $\langle v_i^2 \rangle = \Omega_i J_i$. Passing from this result for time averages for individual stars to population averages over the stars that reach a given place is non-trivial, but it is evident that $\sigma_i^2/\sigma_j^2 = \langle \Omega_i J_i \rangle / \langle \Omega_j J_j \rangle$, where $\langle . \rangle$ is an appropriate average. Essentially all disc stars satisfy Ω_R < Ω_z (Binney 2016), so $\langle J_r \rangle \sim \langle J_z \rangle$ implies σ_R < σ_z.
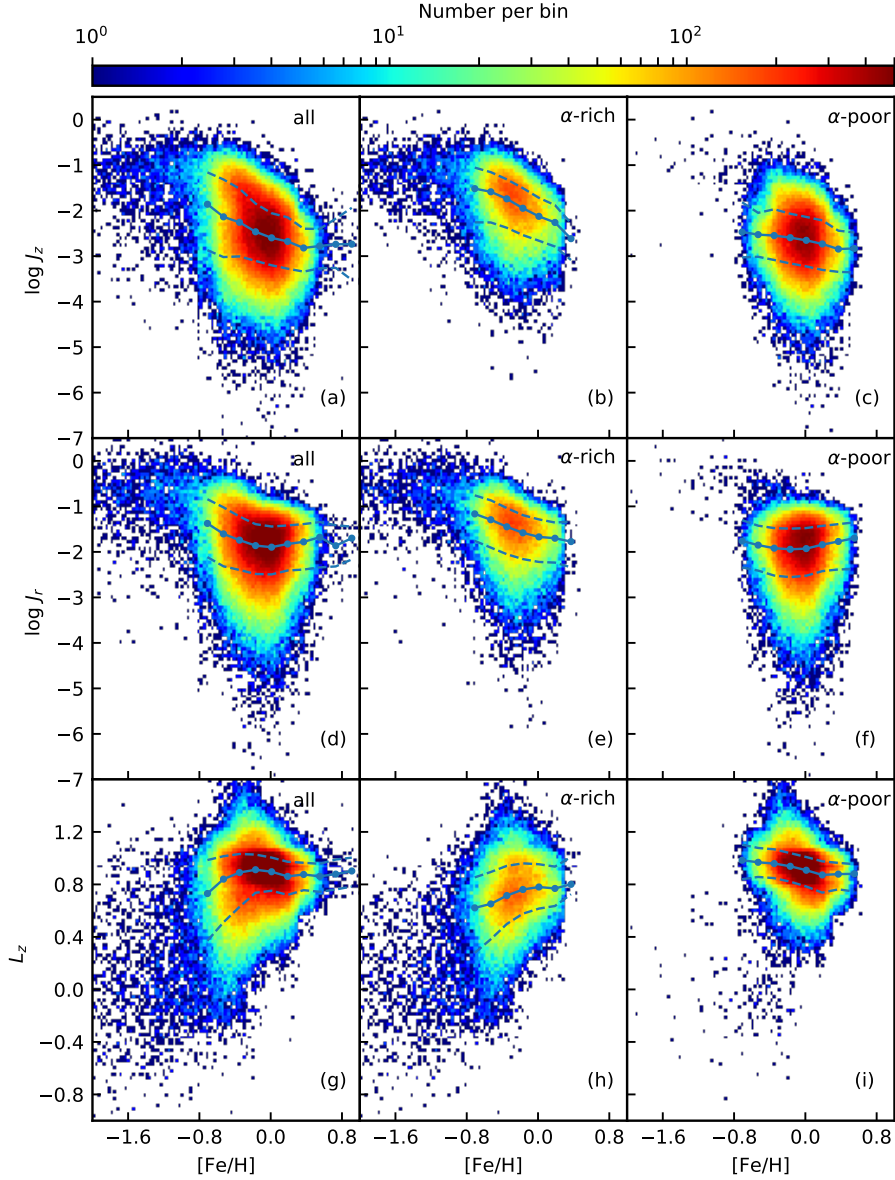
Figure 4. Stellar metallicity vs. actions for overlapping stars between GALAH and *Gaia* DR2 in the 2-kpc diameter volume (Figure 1); the normalised stellar densities are shown in colour. All actions are normalised as discussed in Section 2. The left column is for all stars, the middle column for the α-rich disc, and the right column for the α-poor disc. (a-c) [Fe/H] vs. $\log J_z$, (d-f) [Fe/H] vs. $\log J_R$, (g-i) [Fe/H] vs. $J_\phi \equiv L_z$. The mean trend and 1σ dispersion tracks are also shown in the first column. The L_z split visible in (g) and (i) reflects kinematic substructure within the data.

4   THE PHASE SPIRAL

Antoja et al. (2018) selected stars from *Gaia* DR2 that lie in the thin cylinder $|R - R_0| \leqslant 0.1$ kpc with $|\phi - \phi_0| \leqslant 7.5°$. To revisit the phase spiral in more detail, we expand the volume by an order of magnitude to $|R - R_0| \leqslant 1.0$ kpc and $|\phi - \phi_0| \leqslant 15°$. This expansion ensures that a useful number of GALAH stars are included. As in Antoja et al. (2018), we restrict consideration to stars that satisfy $\sigma_\varpi/\varpi < 0.2$ so that distances can be readily inferred from parallaxes (Schönrich & Dehnen 2018). The domain of our study and that of Antoja et al. (2018) is shown in Figure 1.

Following Antoja et al. (2018), the top left panel of Figure 5 plots the mean value of V_ϕ in the zV_z plane. The overall

tendency is for the centre of the panel to be red, signalling large values of $\langle V_\phi \rangle$, while the edges are blue because there $\langle V_\phi \rangle$ is lower. This overall structure reflects the familiar phenomenon of asymmetric drift: stars that make large vertical excursions (large $|z|$ and/or large $|V_z|$) tend to have guiding centres inside R_0 and are consequently visiting us near apocentre. Superposed on this general trend there is a prominent one-armed spiral of stars with anomalously high V_ϕ. A solid black line has been drawn roughly along the crest of this spiral as follows. A system (r_{ps}, ψ_{ps}) of polar coordinates are defined for the zV_z plane by

$$r_{ps} = \sqrt{(V_z/55 \, \text{km s}^{-1})^2 + z^2}$$
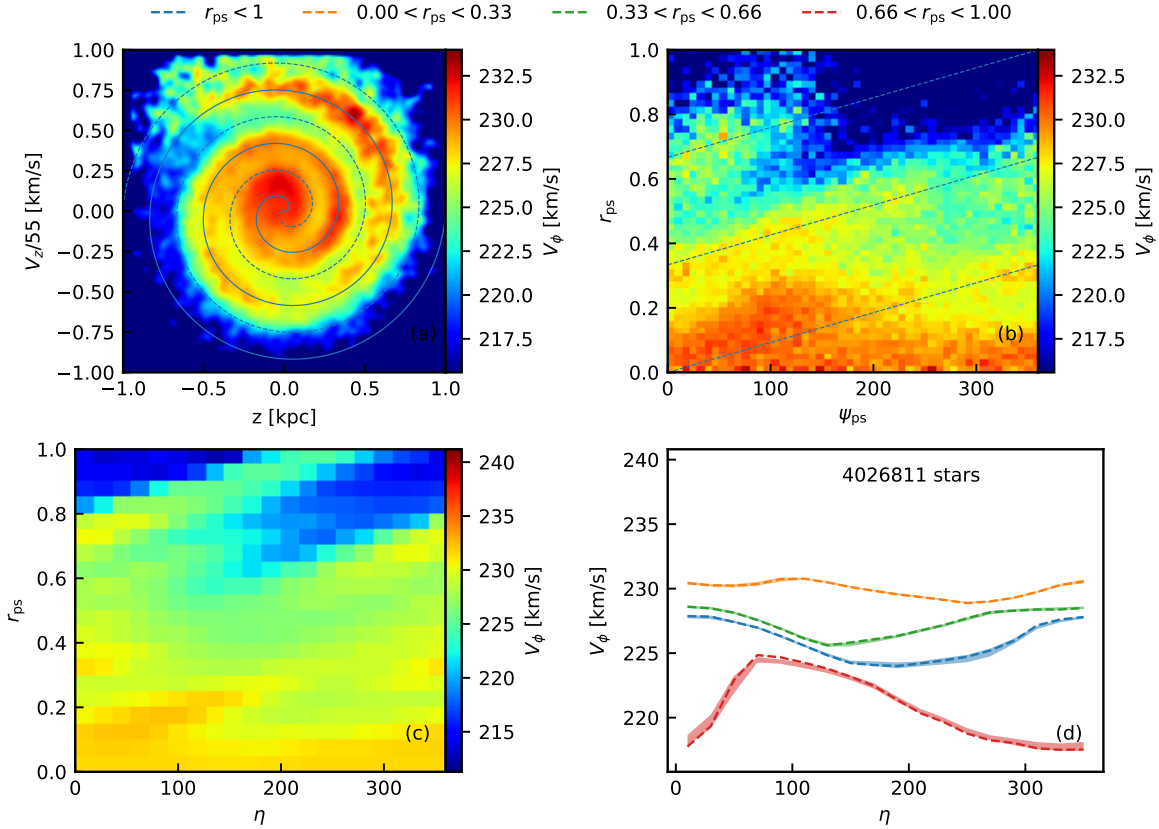
Figure 5. Kinematic properties of stars in the solar neighbourhood using data from *Gaia* DR2. Stars were selected to be within $|R - R_0| < 1.0$ kpc and $|\phi - \phi_0| < 15°$. (a) Map of $\langle V_\phi(z, V_z) \rangle$, i.e. average azimuthal velocity V_ϕ in (z, V_z) plane. Archimedean spirals are overplotted and defined by $r_{ps} = (\psi_{ps} + \eta)/(6\pi)$ with phase angles $\eta = 0$ (solid) and $\eta = 180°$ (dotted). (b) The unwound spiral pattern as a function of r_{ps} and ψ_{ps}. The three diagonal lines are defined for three different radial ranges in (z, V_z) plane. The colour coding is the volume-weighted median azimuthal velocity at each point in (z, V_z). (c) For a fixed spiral pattern, we can plot the same values as a function of r_{ps} and spiral offset angle η; if the archimedean spiral was a good fit to the spiral phase, the bands would be horizontal because the entire spiral would pass through the peak data in (z, V_z) at the same offset angle η. The diagonal banding indicates the fit is not perfect. (d) Median azimuthal velocity as a function of offset angle η for three radial ranges (orange, green, red) as indicated, and where the blue curve is averaged over all radii. The band shows the 68% confidence zone based on bootstrap samples. A well-defined pattern in the data should produce a peak and a minimum in V_ϕ at distinct η values spaced by 180°. As expected, the blue curve peaks at $\eta \approx 0$ with a minimum near $\eta \approx 180°$.

$$\psi_{ps} = \tan^{-1}(V_z/55 \text{ km s}^{-1}, z). \quad (2)$$

where V_z is in units of km s^{-1} and z is in units of kpc. The curve is then the Archimedean spiral

$$r_{ps} = k(\psi_{ps} + \eta) \quad (3)$$

where $k = 1/(6\pi)$ is a constant and $\eta = 0, \pi$ (solid, dashed) allows the spiral to be rotated. The righthand panel of Figure 5 shows how, when $\langle V_\phi \rangle$ is plotted in (r_{ps}, ψ_{ps}) space, the spiral unravels into sloping straight lines that wrap from the right to the left edge of the plot on account of the periodicity of ψ_{ps}.

Within the zV_z plane, stars move clockwise on oval curves that with the adopted scaling $z/\text{kpc} \sim V_z/55 \text{ km s}^{-1}$ are approximately circles. The angular frequency at which a star moves on its circle decreases as the circle's radius increases, so an initially radially directed line of stars is steadily sheared into a spiral like that evident in Figure 5.

Using angle-action coordinates, we can quantify this phase-wrapping process. Figure 6 shows the plane defined
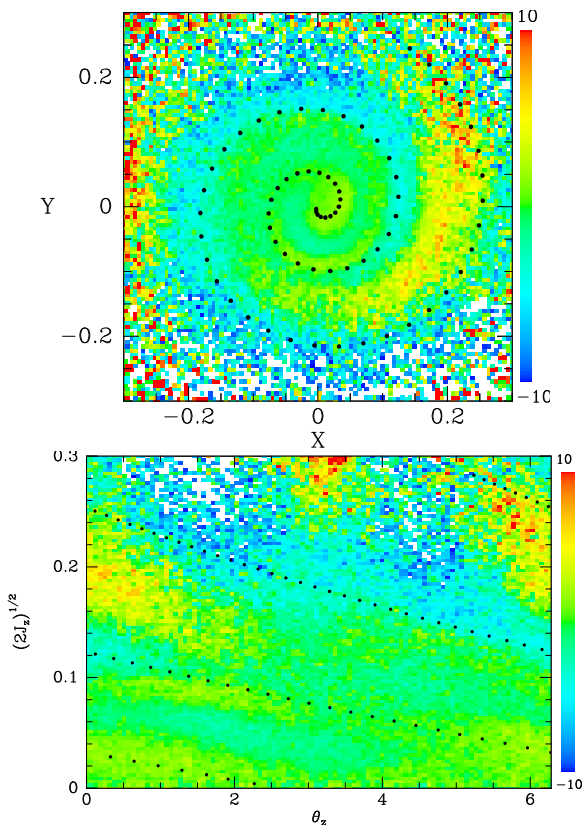
by coordinates

$$X \equiv \sqrt{2J_z} \cos \theta_z \qquad Y \equiv -\sqrt{2J_z} \sin \theta_z, \quad (4)$$

where the minus sign is included in the definition of Y so stars circulate clockwise as θ_z increases.[4] If the stellar z oscillations were harmonic, these coordinates would be simply linearly scaled versions of z and V_z. In reality, they have a complex relation to (z, V_z) because the z oscillations are strongly anharmonic. In the XY plane, stars move exactly on circles of radius $\sqrt{2J_z}$ at the angular velocity Ω_z that can be computed as a function of the radius. The dots in Figure 6 trace the curve

$$\theta_z = \Omega_z(J_{\phi 0}, J_z) t + 0.75 \quad (5)$$

where $J_{\phi 0}$ is the angular momentum of a circular orbit at R_0 and $t = 515$ Myr. This curve delineates quite well the inside

---

[4] The factor 2 in eq. (4) ensures that the area inside a curve of constant J_z is $2\pi J_z$, as it is in the zV_z plane.

Figure 6. Top: the spiral in the angle-action coordinates defined by equation (4). The colour scale shows $\langle V_\phi - \overline{V}_\phi \rangle$, where the overline means the average over θ_z at the given J_r. Bottom: the spiral unwrapped by plotting same quantity in the angle-action coordinates analogous to $(r_{\rm ps}, \psi_{\rm ps})$. The dots show the relation 5,

of the blue spiral. The colour scale in this figure shows the amount by which $\langle V_\phi \rangle$ deviates from its average value around the relevant circle. The spiral, which decreases in amplitude towards the centre, can now be traced all the way to the centre.

Binney & Schönrich (2018) argue that the spiral arises because, at a given value of J_z, the values of Ω_z vary systematically with L_z because stars with smaller guiding-centre radii have higher frequencies. Hence, when some event bunches stars in θ_z, the stars with smaller values of L_z move ahead of the stars with larger L_z as they move around their common circle in the XY plane. The dots in Figure 6 mark the locations reached by stars that lie at the centre of the L_z distribution, so the part of each circle on which V_ϕ is below average should lie at later times on the clock than the part at which V_ϕ is above average. This is precisely what we see in the upper panel of the figure.

4.1 Slicing by location

Figure 7 explores how the properties of the phase spiral vary with location and volume in the Galaxy. Panel (a) exploits the data used by Antoja et al. (2018) that are confined to a narrow vertical cylinder local to the Sun. Panel (b) is the expanded sample around the Sun studied in Figure 5. The volume of the latter sample is twenty times larger than the former, yet the spiral pattern remains essentially the same.

The remaining panels, which also use larger volumes, examine samples in neighbouring spheres close to the solar neighbourhood, two offset to larger and smaller radii (c,d), and two offset in both directions in azimuth (e,f).

As illustrated in Figure 1, panel (c) examines a sample centred at $R = R_0 - 0.5$ kpc, while panel (d) explores a sample centred at $R = R_0 + 0.5$ kpc. The spiral pattern is evident but shows clear differences from inner to outer disc. The inner part of the spiral in (c) is more elongated than in (d) consistent with the stronger disc gravity (see below). The outer part of the phase spiral is more prominent at larger Galactocentric radius.

Panel (e) explores a sample with Galactocentric longitude $|\phi - (\phi_0 + 7.5°)| \leqslant 7.5°$, while panel (f) explores a sample with $|\phi - (\phi_0 - 7.5°)| \leqslant 7.5°$. There is little evolution in azimuth over the inner spiral; the outer spiral is asymmetric in azimuth but not as strongly as in radius.

We also inspected the 2-kpc diameter volume centred at $R = R_0 \pm 1$ kpc; the phase spiral was evident but less well defined due to the smaller number of stars and the larger cumulative errors on measured parameters. *The phase spiral pattern is clearly a disc-wide phenomenon.*

4.2 Slicing by chemistry

In Figure 8, we show how the distribution of stars in the zV_z plane varies with metallicity. On account of the age-metallicity relation, metal-rich stars tend to be younger than metal-poor ones, so by the age-velocity dispersion relation they are more strongly concentrated to the centre of the zV_z plane than metal-poor stars, and especially more than α-rich stars, which, as discussed in Section 3.1, reach exceptionally large values of J_z.

As Figure 9 shows, these differences by chemical composition in the locations of stars within the zV_z plane impact the visibility of the phase spiral in different chemically defined populations. Panel (a) shows the phase plane for α-rich stars in the sense of Figure 3, while panel (b) shows the α-poor stars (cf. Adibekyan et al. 2012). Additionally, we subdivide the α-poor disc into (c) metal poor ([Fe/H]<-0.2) and (d) metal rich ([Fe/H]>0.1) bins. *The phase spiral pattern shows a clear trend in metallicity across the zV_z plane:* for metal-rich stars, the inner spiral is strong; for metal-poor stars, particularly in the α-rich disc, the outer spiral is strong.

The α-rich disc (a) shows much weaker evidence for the phase spiral than the α-poor disc (b), but in part this reflects the order of magnitude smaller size of the sample. To check if this fully accounts for the difference, we examined samples of α-poor stars that were restricted to 31 666 stars by random sub-sampling: even these attenuated samples of α-poor stars showed the spiral more clearly than the α-rich sample. This suggests that the spiral pattern in the α-rich disc is intrinsically weaker than in the colder α-poor disc.

As we vary the metallicity of the α-poor stars under study, two effects are in play. First, on account of the disc's radial metallicity gradient, the mean guiding-centre radius of the sample will decrease as the metallicity is increased, and we saw above (Figure 7) that decreasing the radius weakens the outer spiral. Secondly, by the age-velocity dispersion relation, the zV_z phase covered by the stars will move inwards as metallicity increases (Figure 8), which will again weaken
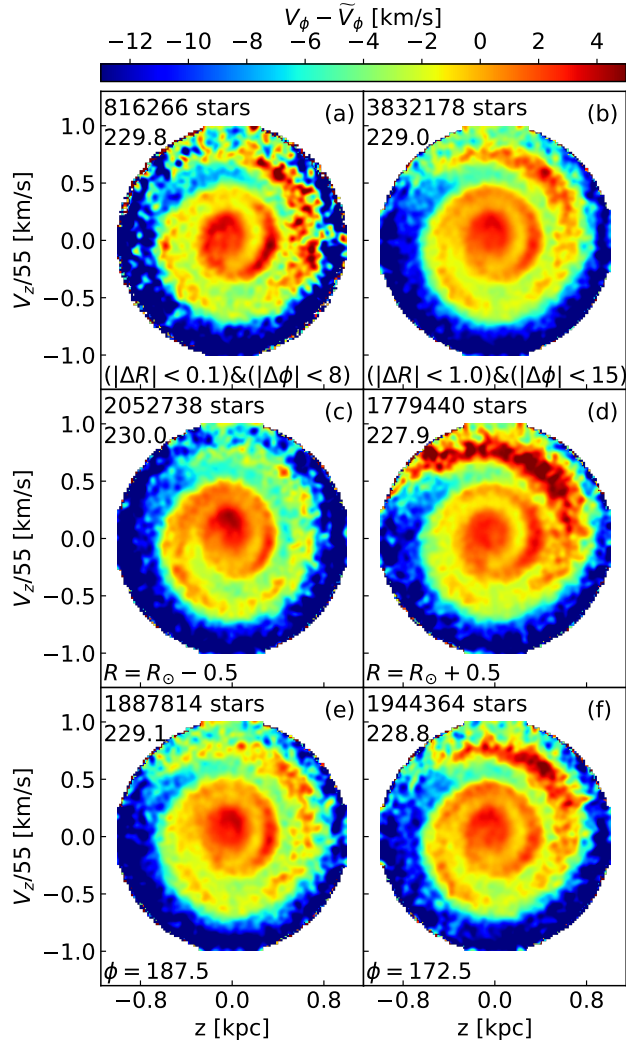
Figure 7. Kinematic properties of stars in the solar neighbourhood in the zV_z plane using data from *Gaia* DR2 explored by volume and location. The colour code shows the deviation in volume-weighted V_ϕ with respect to the median value quoted in each panel along with the number of stars used. (a) Stars with $|R - R_0| < 0.1$ kpc and $|\phi - \phi_0| < 7.5°$ presented in Antoja's original analysis for a narrow vertical cylinder. (b) Stars with $|R - R_0| < 1.0$ kpc and $|\phi - \phi_0| < 15°$ highlighting the same phase spiral over the 20× larger GALAH volume. (c) Stars with $(|R - (R_0 - 0.5)| < 1.0$ kpc and $|\phi - \phi_0| < 15°$. (d) Stars with $|R - (R_0 + 0.5)| < 1.0$ kpc and $|\phi - \phi_0| < 15°$. Note the inner spiral in (c) is vertically elongated consistent with the smaller Galactic radius; the outer spiral in (d) is more prominent at larger radius. (e) Stars with $|R - R_0| < 1.0$ kpc and $|\phi - (\phi_0 + 7.5°)| < 7.5°$. (f) Stars with $|R - R_0| < 1.0$ kpc and $|\phi - (\phi_0 - 7.5°)| < 7.5°$. Note the slight asymmetry in azimuth as well as radius in the prominence of the outer spiral.

the spiral (Figure 6). In line with these expectations, in Figure 9, the outer spiral is clearest for the most metal poor stars (c) and becomes weaker as we increase the metallicity of the sample (d).

The trend in the spiral pattern with metallicity is smoothly varying with no evidence for a chemically homoge-
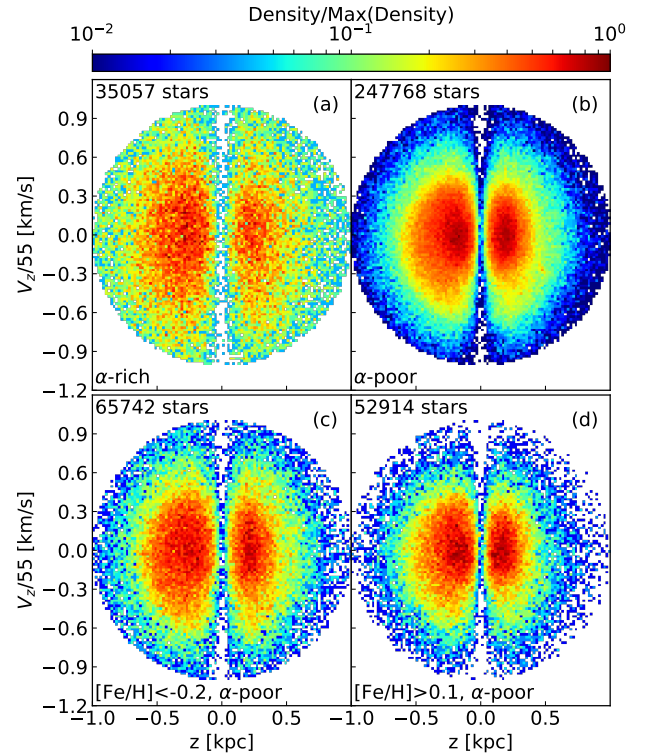
Figure 8. The density of GALAH stars in the zV_z plane as a function of metallicity: (a) α-rich disc, (b) α-poor disc, (c) α-poor, metal-poor disc, (d) α-poor, metal-rich disc. The number of stars used in each panel is indicated.

neous or single-age population (e.g. star cluster) dominating the phase spiral at fixed V_ϕ.

4.2.1 *LAMOST analysis*

To stress the robustness of the phase spiral signature, we show that it can be extracted from the LAMOST survey (Deng et al. 2012). LAMOST (Large Sky Area Multi-object Survey Telescope), based in Hibei Province in China, is a lower spectral resolution ($R \sim 1800$) survey but has observed a far greater number of stars than other ground-based surveys, with over 5 million stellar spectra collected to date. The third data release, with data for $\sim$ 1.5 milion stars (LAMOST DR3), is available at https://dr3.lamost.org. The database does not supply [α/Fe] ratios so we are unable to separate the α-poor and α-rich discs, but the survey is dominated by the former (i.e. local thin disc), so the $V_\phi(z, V_z)$ results presented in Figure 10 are best compared to the GALAH data for the α-poor disc (Figure 9(b-d)). We note two things: (i) a weak phase spiral is evident, and (ii) the panels (a) and (b) broadly resemble the GALAH results in Figure 9(c) and (d) respectively.

4.3 Slicing by actions

In Figure 11, we explore how the zV_z phase plane varies when stars are selected by the values of their actions J_r and L_z. Stars are split by whether their radial action is greater
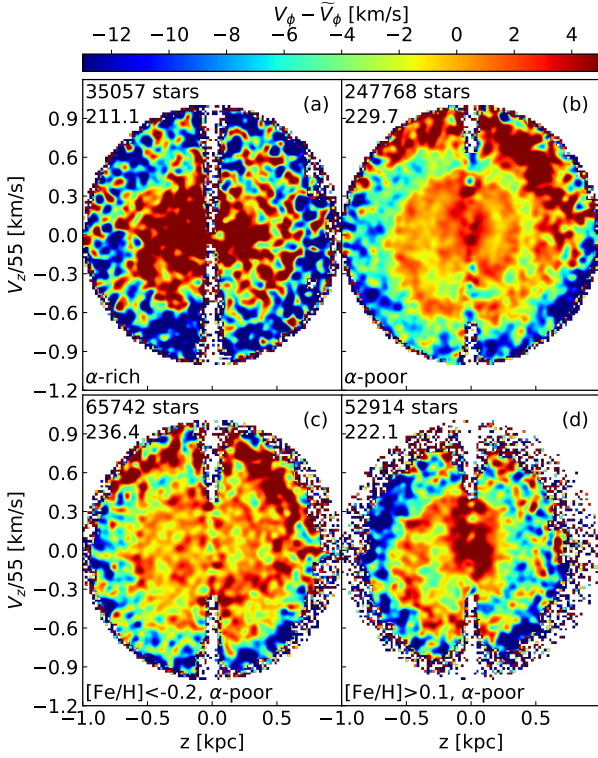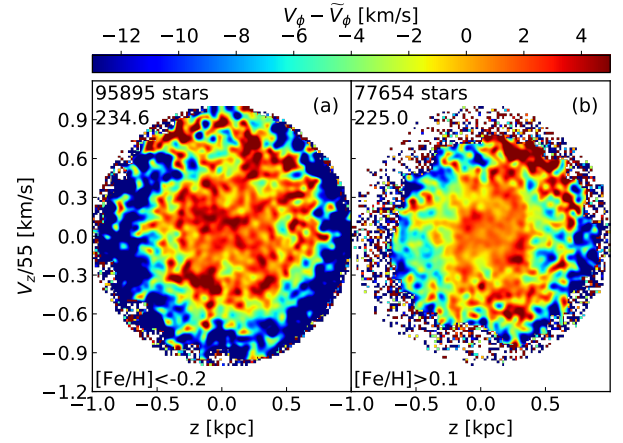
Figure 9. Kinematic properties of stars in the solar neighborhood in the zV_z plane using overlapping data from GALAH and *Gaia* DR2 in the expanded local volume. The four panels match the four density panels in Figure 8. We show the dependence of the phase spiral on metallicity: (a) α-rich disc, (b) α-poor disc, (c) α-poor, metal-poor disc, (d) α-poor, metal-rich disc. The number of stars used in each panel is indicated. In panel (d), the inner phase spiral is prominent in the younger, α-poor, metal-rich disc, but is not obviously evident in the older stars, i.e. the α-rich disc and the α-poor, metal-poor disc (a,c). The outer spiral is most prominent in the α-poor, metal-poor disc (b,c).

Figure 10. Kinematic properties of stars in the solar neighborhood using data from LAMOST DR3 and *Gaia* DR2 sampled over the sample expanded volume used for GALAH stars. Unlike GALAH, LAMOST DR3 does not provide [α/Fe] estimates, so the splits are made on [Fe/H]. The phase spiral is barely evident at low contrast in both panels and broadly resembles the respective GALAH-defined panels in Figure 9.

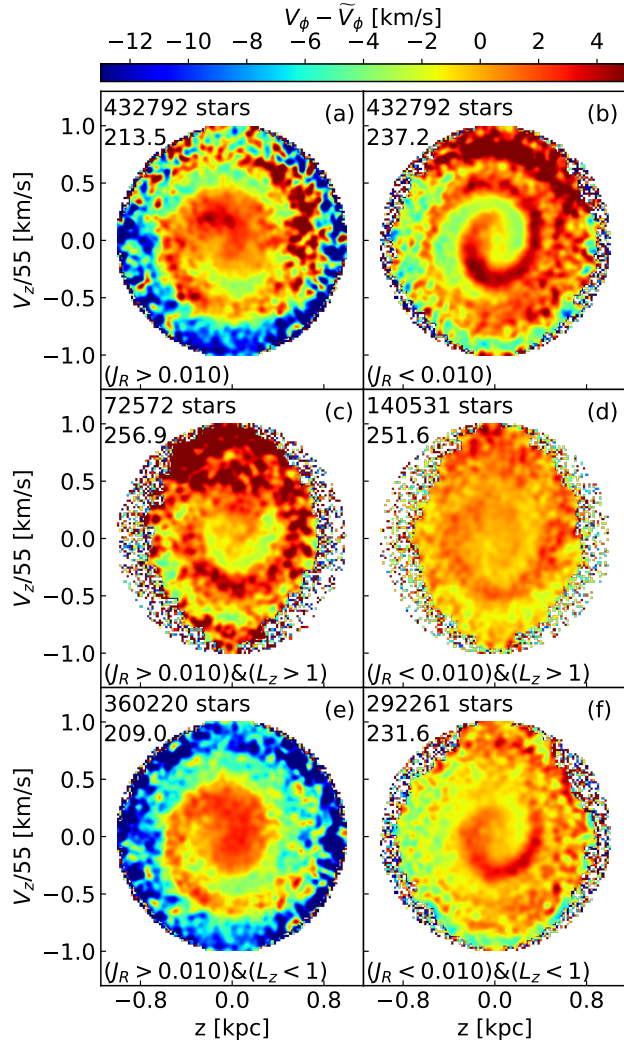very far from relaxed, with a strong bias towards values of $\psi_{\rm ps} \sim 90°$.

4.4 Slicing by ages

The *Gaia* DR2 data release provides accurate photometry in three bands that we exploit here, i.e. the super-broadband G filter, and for the split bands $G_{\rm BP}$ (blue) and $G_{\rm RP}$ (red) (Jordi et al. 2010). We use the *Gaia* colour ($G_{\rm BP}$-$G_{\rm RP}$) to estimate crude photometric stellar ages. *Gaia* also provides a reddening estimate; we use these to demonstrate some problems but do not use them in the final analysis. First, they are not available for all stars. Secondly, for the bluest stars, the velocity dispersion is found to be larger for dereddened colors as compared to unreddened colours, indicating that for blue colours, there is contamination from older stars.

To calibrate the age-colour relation, we use `Galaxia` to generate a mock catalog for all stars in the GALAH volume and derive *Gaia* magnitudes and colours. `Galaxia` uses Bayesian estimation using a scheme that takes into account the initial mass function, the star formation rate and a sophisticated treatment for dust extinction (Sharma et al. 2011; Sharma 2017). In Figure 12, The resulting raw distribution closely matches the *Gaia* data over the same volume. The dust-corrected photometry matches less well because the *Gaia* photometry with dust corrections represent a biassed sample that is not accounted for in the `Galaxia` model.

In Figure 13, we derive a median age as a function of $G_{\rm BP}$-$G_{\rm RP}$; the 16 and 84 percentile ranges are also shown. The profiles are given for both the extinction-corrected and uncorrected colours, both of which show a monotonic increase in age with colour up to $G_{\rm BP}$-$G_{\rm RP} \approx 0.75$ (3 Gyr). Beyond here, the *Gaia* colour is a poor tracer of age. The separation of giants and dwarfs is shown in Figure 12. We select dwarfs as $M_G < 3.5(G_{\rm BP}$-$G_{\rm RP}$-0.15$)$, where M_G is the abso-

than (left panels: a,c,e) or less than (right panels: b,d,f) the median value over the *Gaia* volume, $\tilde{J}_r = 0.01$. Stars with larger J_r move on more eccentric orbits. Near the centre of the phase plane, the spiral is much more clearly traced by stars with less eccentric orbits. In fact, panels (b) and (f) provide *the clearest manifestation to date that the phase spiral can be traced to the origin of the vertical phase plane.* Notice that the V_ϕ scales of the two panels are quite different, so V_ϕ for the low-eccentricity stars is systematically larger than for the high-eccentricity stars. This indicates that stars with large J_r typically have guiding-centre radii inside R_0, a consequence of both the steep radial density gradient within the disc and the outward decline in σ_R.

The lower row in Figure 11 shows the effect of further splitting stars by their values of $L_z \equiv J_\phi$. The guiding centres of stars with $L_z > 1$ lie outside R_0, and conversely for stars with $L_z < 1$. Comparison of panels (d) and (f) shows significant difference in the structure of the innermost portion of the phase spiral – stars with smaller L_z form a tighter spiral that reaches the centre sooner. Panel (c) shows that the stars on eccentric orbits with large guiding centres are

Figure 11. An analysis of actions (J_R, $J_\phi \equiv L_z$) over the original Antoja volume ($|\Delta R| < 0.1$ kpc). The left panels show stars with $J_R > \tilde{J}_R$, where $\tilde{J}_R$ is the median value over the volume. The right panels show stars with $J_R < \tilde{J}_R$. The character of the phase spiral is very different for stars with eccentric (a) compared to circular (b) orbits. Thus, we divide the distribution in action further: (c) $J_R > \tilde{J}_R$, $L_z > 1$; (d) $J_R < \tilde{J}_R$, $L_z > 1$; (e) $J_R > \tilde{J}_R$, $L_z < 1$; (f) $J_R < \tilde{J}_R$, $L_z < 1$. Stars with $L_z > 1$ have guiding-centre radii outside the Solar Circle. Comparison of panels (f) and (d) reveals the tight inner spiral arises from stars with less eccentric orbits with guiding radii inside R_0 that reach apogalacticon in the solar neighbourhood. Comparison of panels (c) and (e) shows that stars on eccentric orbits from the outer disc are much less relaxed.

lute magnitude derived using *G*-band photometry and the parallax-derived distance.

In Figure 14, we show the $\langle V_\phi(z, V_z) \rangle$ map in the vertical phase plane for dwarfs and giants. The dwarfs are further split up into three different age slices. The vertical extent increases with age due to the age-velocity dispersion relation. The giants and the oldest dwarfs have a similar distribution in age but the the oldest stars are restricted in z as compared to giants because of the selection function limit ($G < 14$): red
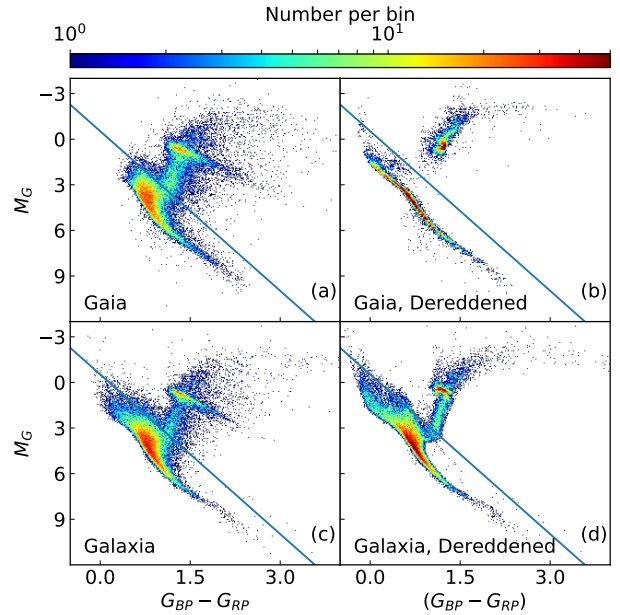

Figure 12. The colour-magnitude distribution of *Gaia* stars in the solar neighborhood and that of a mock sample generated with the `Galaxia` model for the Galaxy (Sharma et al. 2011) which includes a sophisticated treatment of the dust extinction. The *Gaia* sample is similar to that used by Antoja et al. (2018) and consists of stars with valid radial velocities, less than 20% error on parallax, $|\Delta R < 1.0|$ kpc, $|\Delta\phi| < 15°$, and $|\Delta z| < 1$ kpc. The mock sample was generated to match the *G* magnitude distribution and the selection criteria of the *Gaia* sample. Qualitatively, the raw counts in the colour-magnitude diagram uncorrected for dust extinction agree very well. The dereddened data and models agree less well because the dereddened *Gaia* stars are a biassed sample; we do not use this sample in our analysis. The diagonal blue line is how we separate giants (upper) from dwarfs (lower); see the main text.

dwarfs are intrinsically fainter and harder to detect at high z.

For the dwarfs, the spiral pattern exhibits a systematic trend with age. The inner 'hook' of the phase spiral is stronger and clearer for stars younger than 3 Gyr; for older stars, the centre is more filled in. The 16 and 84 percentile age range for giants is about 1 to 9 Gyr, with a median age of 3.4 Gyr. The old dwarfs and giants have a similar distribution in the zV_z plane although the outer phase spiral for giants is more diffuse presumably because they arise from a larger volume in (R, z). For younger dwarfs (Figure 14b,c), the inner hook closely resembles that of stars with $J_R < 0.01$ (Figure 11b) as expected as these are stars on more circular orbits.

This raises an important question. Were the younger stars perturbed or kicked into the spiral pattern after they were born, or did they form from gas which was perturbed into the spiral pattern? If the former, this suggests that it is more difficult to excite a spiral pattern within an old, dynamically hot population. Conversely, if the latter applies, this may mean the pattern is stronger and more coherent in the gas phase. Given that collisionless stars and gas respond slightly differently to a perturbation in the potential, the
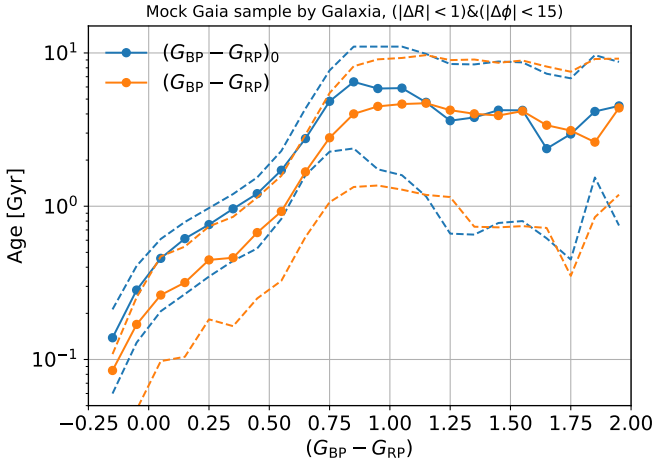
Figure 13. Given the assumed model and selection function for the Galaxy in Figure 12 , we derive a mean stellar age as a function of the *Gaia* colour. The lower solid curve is based on the raw *Gaia* photometric data uncorrected for dust extinction; the 16 and 84 percentile ranges are shown as dashed lines. The upper curves are the *Gaia* photometric data corrected for dust extinction. There is no age discrimination beyond about 3.5 Gyr.

two scenarios may lead to different phase distributions for the younger stars. In a later paper, we test these ideas using an N-body simulation that has a disc continuously forming stars while interacting with the Sgr dwarf.

5 V_R AND THE VELOCITY ELLIPSOID

5.1   Tilt of the velocity ellipsoid

The top panel of Figure 15 plots $\langle V_R \rangle$ in the phase plane. On the largest scale a quadrupole pattern is evident, with $\langle V_R \rangle$ becoming large at top left and bottom right, and small at top right and bottom left. The bottom panel illustrates the origin of the quadrupole by showing a typical orbit in the (meridional) Rz plane. At upper left of the top panel, a star is below the plane and moving up. Hence in the bottom panel it is at a location like those marked by red arrows. By conservation of energy the star's speed in the Rz plane is the same, whether V_R is positive or negative. But because the right and left running trajectories do not make the same angle with the vertical, the absolute magnitudes of V_R differ at the two phases: the larger value corresponds to the phase that is carrying the star outwards. So averaging over all stars below the plane and moving up we expect $\langle V_R \rangle > 0$ just as the top panel reveals. When this analysis is repeated for the upper right part of the top panel, so for stars that are above the plane and moving up, the relevant phases in the bottom panel are marked with blue arrows, and now the negative value of V_R is dominant.

Averaged over billions of stars, the microphysics just described gives rise to the well-known tilt of the velocity ellipsoid as one goes above or below the plane: at $z = 0$ the long axis of the velocity ellipsoid is aligned with the centre-anti-centre line. Off the plane, the long axis tips almost as
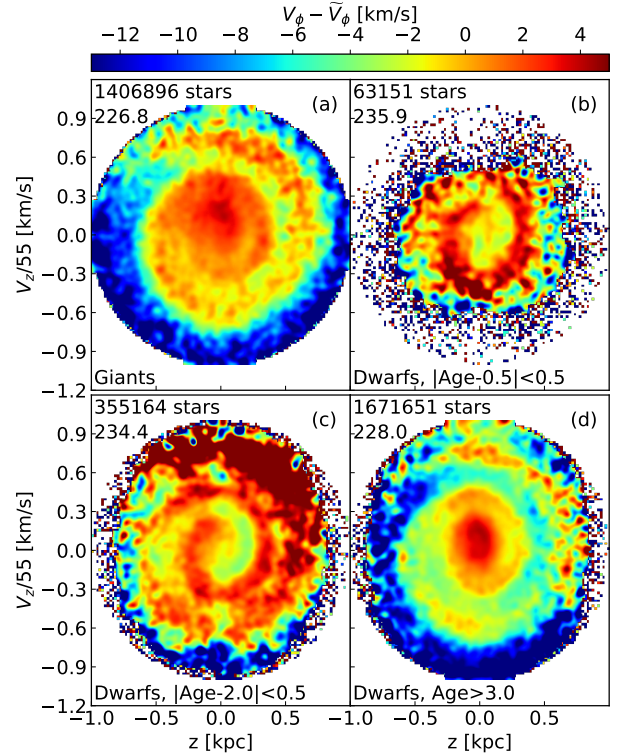

Figure 14. An analysis of the *Gaia* photometry over the GALAH volume in the zV_z plane showing crude stellar ages for (a) giants and (b-d) dwarfs. Stars younger than about 2.5 Gyr emphasise the 'hook' at the centre of the phase spiral (b,c). This feature closely resembles Figure 11b for which $J_R < 0.01$, i.e. younger stars from the local disc are on more circular orbits. The giants (a) and the old dwarfs (d) resemble Figure 11a for which $J_R > 0.01$, i.e. the older stars are on more elliptic orbits. Interestingly, dwarfs at large r_{ps} in (d) are restricted to a thinner phase spiral than the giant population in (a).

much as is required for it to continue to point towards the Galactic centre (Siebert et al. 2008; Binney et al. 2014). An illustration of the effect is given in Figure 16 along with a simulation of the quadrupole in Figure 17 extracted from the galaxy simulations in Sec. 7. Hence the quadrupole shown by Figure 15 in the *Gaia* DR2 stars is a novel signature of the velocity ellipsoid's tilt. It should have been anticipated but seems not to have been.

5.2   The spiral in V_R

The most prominent feature of Figure 15 is a spiral observed in $\langle V_R(z, V_z) \rangle$ that is broadly similar to that in $\langle V_\phi \rangle$ (Figure 5 and Figure 6). In detail, the spirals differ: near the centre the V_R spiral is less tightly wound than the V_ϕ spiral. In Figure 18, we dissect the plane along the same lines as Figure 7. Once again, the V_R spiral pattern in Antoja's original volume (a) is recovered in the 20× larger GALAH volume in (b). Interestingly, the inner spiral does not vary greatly with location, either in radius (c,d) or in azimuth (e,f). But the quadrupole pattern is substantially stronger over the inner disc compared to the outer disc; there is no gradient in az-
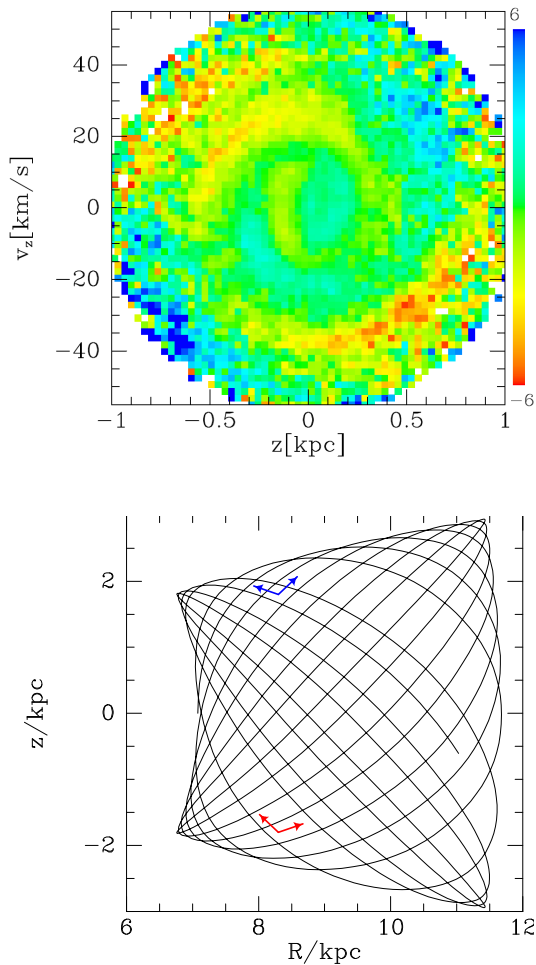
Figure 15. Top: $\langle V_R \rangle$ plotted in the phase plane. A quadrupole pattern (blue top left and bottom right, red bottom left and top right; need to change sign of image) dominates the outer portion of the circle. Towards the centre the spiral is clearly visible. Bottom: a typical orbit in the Rz plane. A point at upper left of the top panel corresponds to phases associated with the red arrows in the bottom panel, while a point at upper right of the top panel is associated with the blue arrows in the bottom panel.

imuth. These are real variations as reflected in the matched star counts in each panel.

In Figure 19, we use the GALAH data to dissect the phase spiral in V_R by chemistry. The quadrupole pattern is evident in all panels and tends to obscure the phase spiral. The latter is most evident in the panel for the summed α-poor disc (b). Thus the spiral in $\langle V_R \rangle$ is manifested in the same populations as as the spiral in $\langle V_\phi \rangle$ as we would expect if it is simply another aspect of a common dynamical phenomenon as Binney & Schönrich (2018) argue.

6   DYNAMICAL INTERPRETATION

In Sections 4 and 5, we have encountered abundant evidence that the phase spiral is present over a wide extent in radius and involves stars of many ages and chemical compositions. Hence it definitely does not arise through phase mixing of stars born in a massive starburst (Candlish et al.

2014). Rather it is an extension to the zV_z plane of one of the most important discoveries in *Hipparcos* data: the detection by Dehnen (1998) of clumps in the UV plane. The traditional explanation of such 'star streams' is that they are dissolving star clusters, but from the work of Dehnen (1998) and Famaey et al. (2005), it became clear that the clumps in the UV plane were heterogeneous in age and metallicity so they could not comprise stars that formed together, but must have been swept up by some dynamical process. The GALAH data establish that the stars that make up the zV_z spiral do not have a common origin but have been likewise caught up in a dynamical process. To a first approximation, the Galactic disc is an axisymmetric equilibrium structure. The data now at hand force us to move on from this starting point to consider the effects on non-axisymmetric and non-stationary perturbations.

Antoja et al. (2018) showed examples of an initial clump of stars in the zV_z plane winding up into a phase spiral as they move in a toy anharmonic potential $\Phi(z) = az^2 + bz^4$. Binney & Schönrich (2018) pointed out that this model does not explain why the spiral is not evident in a plot of the density of Gaia DR2 stars in the zV_z plane but emerges clearly when $\langle V_\phi \rangle$ is plotted. They argued that the keys to understanding this phenomenon are (i) that Ω_z is a strong function of L_z as well as of J_z so stars are sorted by L_z as they progress around the zV_z plane, and (ii) that when an intruder such as the Sgr dwarf crosses the plane, oscillations are initialised in both the in-plane and perpendicular directions. That is, the observed spiral is the result of two independent but synchronised oscillations.

Binney & Schönrich (2018) presented a toy model of the impact of an intruder crossing the disc. They made the model tractable by using the impulse approximation to compute the disturbance that the intruder causes. While recognising that the impulse approximation would in this case be invalid, they argued that errors introduced by it are smaller than those introduced by neglect of the perturbations to the Galaxy's gravitational potential that arise as the disc responds to its initial stimulus. Notwithstanding its weaknesses, their toy model reproduced for the first time spirals in $\langle V_\phi \rangle$ and $\langle V_R \rangle$ with plausible parameters for the mass and location of the intruder.

The deficiencies of the perturbative treatment of Binney & Schönrich (2018) cannot be addressed until there is a major breakthrough in the theory of disc dynamics. It is intuitively clear that if we could solve the equations of linearised perturbation for a self-gravitating stellar disc, at least two wave modes would emerge: in one mode the disturbance would be largely parallel to the plane and be associated with spiral structure, and in the other mode the perturbation would be largely perpendicular to the plane and would be associated with warps and corrugation waves.

After decades of frustration, we now have in the work of Goldreich & Lynden-Bell (1965), Toomre (1981, 1969), Sellwood & Carlberg (2014) and Fouvry et al. (2015) a convincing theory of the dynamics of razor-thin discs. Noise from any source, including Poisson noise, generates leading spiral waves, which are swing amplified near their corotation resonance and subsequently absorbed by Landau damping at a Lindblad resonance. The disc is heated by the absorption in an annulus that is typically very narrow, and as a consequence the impedance of the disc to propagating spi-
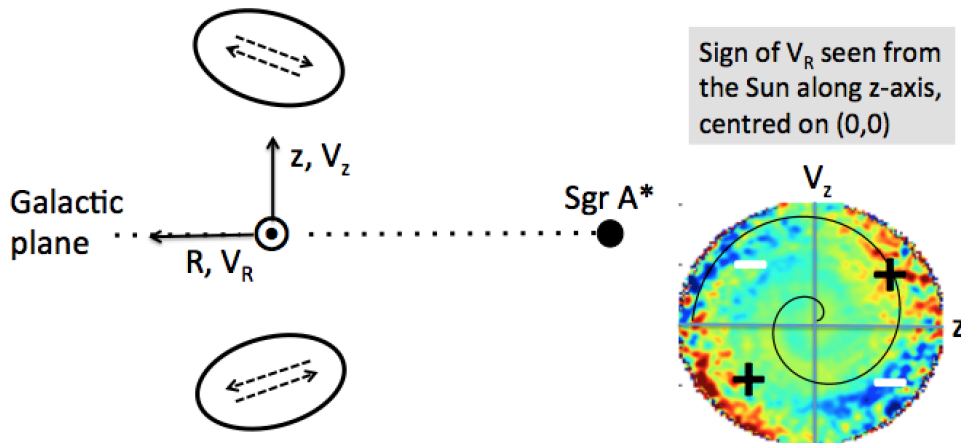
Figure 16. (Left) The adopted coordinate frame in phase space defined with respect to the Galactic cylindrical coordinates shown with respect to the Sun's position. The tilted velocity ellipsoids above and below the Galactic plane are also indicated. The dashed arrows show the direction of the fastest motions within the ellipsoid. (Right) When viewed from the Sun, the tilted velocity ellipsoids produce a characteristic quadrupole ∓± pattern as seen in the GALAH and *Gaia* data. The data are taken from Figure 18; see the text for further discussion.
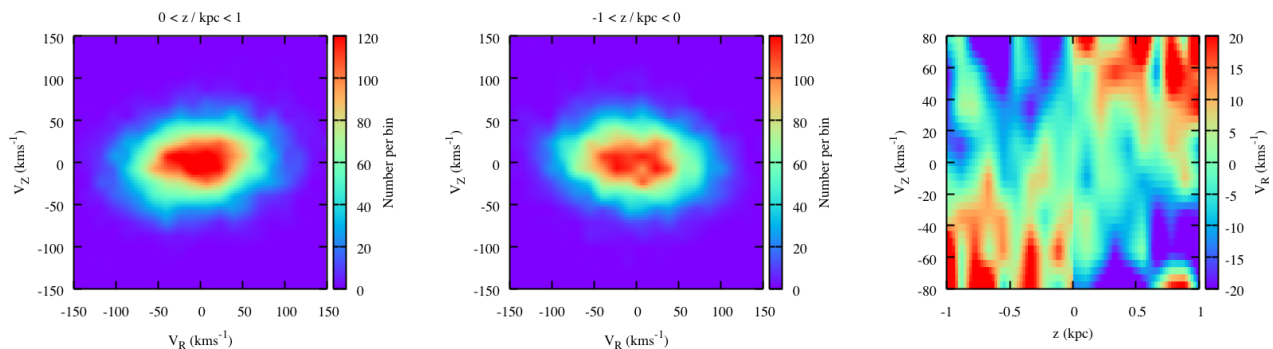
Figure 17. Velocity ellipsoid for star particles in the unperturbed Galaxy model above (left) and below (centre) the disc plane. The right panel shows the phase space distribution $\langle V_R(z, V_z) \rangle$ corresponding to the panels to the left. Compare these figures with Figure 16. Note that the tilt of the ellipsoid in each case here is mirrored with respect to the vertical axis compared to the corresponding ellipsoid in Figure 16 because the $R - z$ reference system (implicit in the left and central panels) is mirrored in the same way.

ral waves is caused to vary on small scales. When a wave propagating from its corotation to its Lindblad resonance subsequently hits such a region, it is partially reflected back to corotation to be re-amplified. Gradually, as the disc ages and the number of these narrow regions grows, significant fractions of swing-amplified waves are reflected by some feature back to corotation to be re-amplified before they can reach their Lindblad resonance and be absorbed. Hence the disc's responsiveness to stimulation by noise steadily grows until the disc becomes simply unstable. At that point the spiral structure becomes an O(1) phenomenon and a bar forms.

The picture just described certainly marks a significant step forward in understanding galaxies, but it falls short of what is required to address the data we now have because it is confined to razor-thin discs. It is clear that the fundamentally in-plane mode must involve V_z in addition to V_ϕ because stars will be drawn down to regions of high density.

That is, a propagating spiral arm will force oscillations perpendicular to the disc that satisfy the symmetry condition $V_z(-z) = -V_z(z)$. These motions will remain conjectural until the theory of spiral structure has been extended from razor-thin discs, in which vertical motion is impossible, to discs of finite thickness. This extension proves extremely difficult (Fouvry et al. 2017).

The available formalism relating to the second kind of mode, corrugation waves, is even more primitive than the current theory of spiral structure because it involves neglecting epicycle oscillations in addition to taking the disc to be razor thin (Hunter & Toomre 1969). Hence we really have very little idea what a proper theory of corrugation waves would look like. We do, however, know that their z motions would satisfy the symmetry condition $V_z(-z) = V_z(z)$ and they will almost certainly involve V_ϕ in addition to V_z because warps are all about torques exerted by one ring on another.

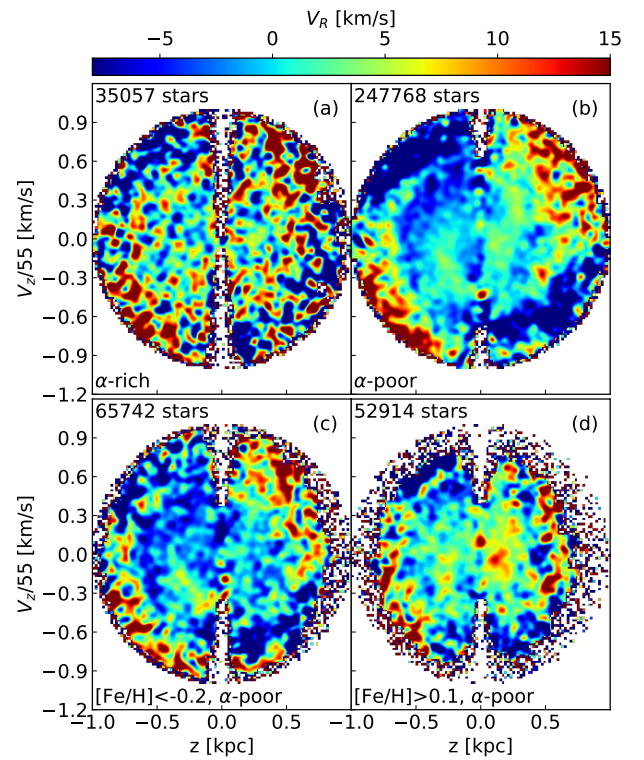In these circumstances, the natural thing to do is to re-
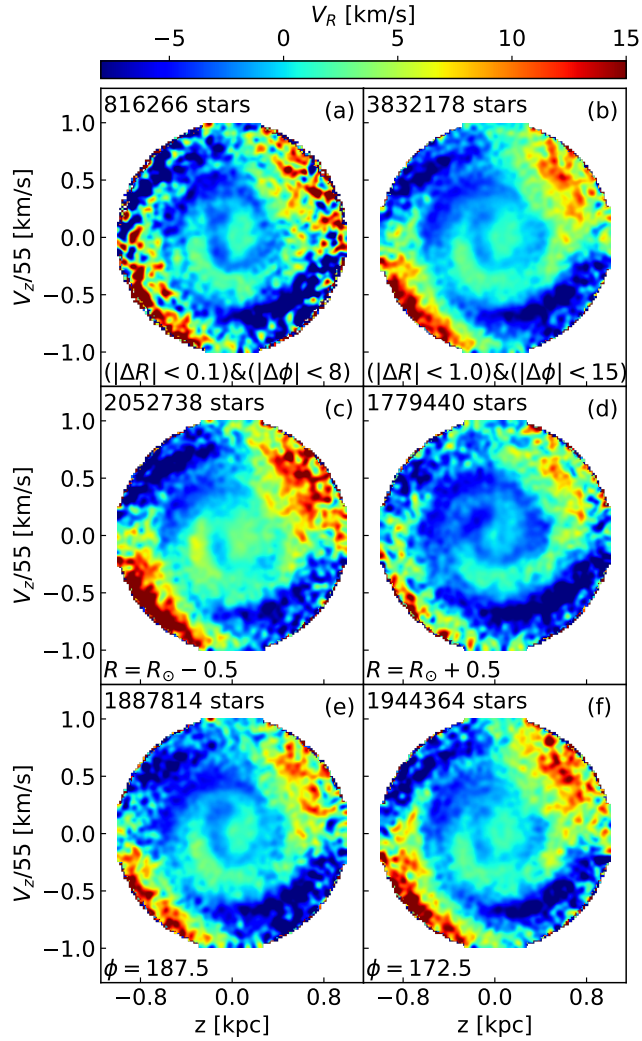
Figure 18. Map of median V_R in (z, V_z) plane for stars in the solar neighbourhood using data from *Gaia* DR2. The sample definitions are the same as in Figure 7. The quadrupole defined by the sign changes in each quadrant are due to the tilt of the velocity ellipsoid (see the sketch in Figure 16). Note that a weak phase spiral pattern is visible in the center. The pattern is stronger for the $R = R_0 - 0.5$ case as compared to $R = R_0 + 0.5$ case.

Figure 19. Map of median V_R in (z, V_z) plane for stars in the solar neighbourhood using data from GALAH and *Gaia* DR2. The sample definitions are the same as in Figure 9.

Table 1. Galaxy model parameters. Column headers are as follows: M_t := total mass (10^9 $M_\odot$); r_s := scalelength (kpc); r_{tr} := truncation radius (kpc); N_p := number of particles (10^5).

	Profile	M_t	r_s	r_{tr}	N_p
Galaxy					
DM halo	H	10^3	38.4	250	10
Bulge	H	9	0.7	4	3
Thick disc	MN	20	5.0^a	20	6
Thin disc	Exp/Sech	28	5.0^b	20	10

Notes. H := Hernquist (1990) profile; MN := Miyamoto & Nagai (1975) profile; Exp := radial exponential profile.; Sech := vertical sech$^2 z$ profile.
[a]scaleheight set to 0.5 kpc.
[b]scaleheight set to 0.3 kpc.

sort to N-body simulation. As we shall see, modelling the *Gaia* DR2 data in this way is extremely challenging because one needs to achieve high resolution in the small part of the 6D phase space in which the spiral is detected, while at the same time resolving the dynamic (live) dark halo, which we expect to participate in the excitations under study and extends to beyond 100 kpc, sufficiently to prevent it becoming an important source of artificial Poisson noise.

7 N-BODY SIMULATIONS

In a recent paper, Tepper-García & Bland-Hawthorn (2018) examine the impact of Sgr on the Galaxy with an N-body, hydrodynamical simulation that has the unique feature of including a gas component demanded by the resolved star-

formation history of the dwarf. This work, which used the adaptive mesh refinement (AMR) gravito-hydrodynamics code Ramses (version 3.0 of the code described by Teyssier 2002), emphasized that the number of disc crossings and the timing of Sgr's orbit depend on the rate at which Sgr loses dark and baryonic mass. Here we re-run these models without the gas component using an updated Galaxy model (Table 1) with extended ranges of intruder mass and orbit parameters (Table 2). Our simulations contain almost three million particles, of which 1.6 million are disc stars and one million are dark-matter particles.
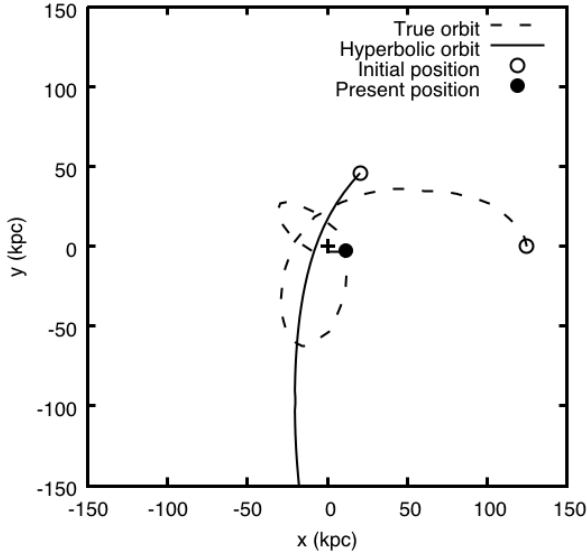
Figure 20. The projection of the polar orbits for the intruders with different mass (hyperbolic vs. realistic) into the (x, y) plane seen from the NGP. The cross indicates the Galactic Centre. The dashed line shows the complex 'trefoil' orbit of Sgr over the past 2.3 Gyr, now accepted across many studies since Law et al. (2005). Sgr (shown as a filled circle) crossed the disc about 420 Myr ago at $R = 13$ kpc and is due to transit again in about 50 Myr. For more details, see Tepper-García & Bland-Hawthorn (2018).

Table 2. Overview of intruder models. Column headers are as follows: M_{tot} := total mass (10^9 M$_\odot$); M_{tid} := tidal mass (10^9 M$_\odot$); r_{tr} := truncation radius (kpc); N_p := number of particles (10^5). The last column gives the approximate initial orbital speed (km s^{-1}). See the notes below the table for more information.

Model	M_{tot}	M_{tid}	r_{tr}	N_p	v_0
K (high mass, Sgr orbit)	100	90	60	5	80
L (intermediate mass, Sgr orbit)	50	40	45	5	80
M (low mass, Sgr orbit)	10	7	25	5	80
R (high mass, single cross)	100	60	24	2	370
S (intermediate mass, single cross)	50	30	19	1	360
T (low mass, single cross)	10	5	12	1	350

We include a simulation of an unperturbed disc to emphasize the long-term stability of our models. In addition to the realistic Sgr orbit models with their multiple crossings, we also simulate intruders crossing the disc along (unrealistic) hyperbolic orbits to study the disc's response to a strong, one-time impulsive transit. The face-on projection of both orbits shown in Figure 20 suggests that with the realistic orbit successive crossings may influence the coherence and longevity of the phase spiral.

Appendix A summarises the content of movies of these simulations that are available at `www.physics.usyd.edu.au/~tepper/proj_galah_paper.html`. There are movies to show both configuration space and phase space. We practice an open policy on set-up files for all of our N-body + MHD studies to encourage cross checking, and encourage others to do the same.

Below we provide plots in the zV_z phase plane for particles that are widely distributed in L_z. Figure 21 helps us to understand the basic structure of these plots. Its top six panels show curves of constant J_z in the zV_z plane for orbits with circular angular momentum and small radial action at radii that decrease from $R = 20$ kpc at top left to $R = 5$ kpc at bottom right. The values of J_z for which curves are plotted are the same in each panel. As one moves inwards, the curves become steadily more elongated vertically, while their area, which is equal to $2\pi J_z$, remains constant because the set of J_z values is the same in every panel. These orbit traces stretch along the V_z axis while shrinking along the z axis in consequence of growth in the vertical restoring force K_z as R decreases and the surface density of the disc increases. The lower four panels of Figure 21 show the extent of phase wrapping in a given time (250 Myr). As R shrinks, Ω_z increases and an initially radially directed straight line in the phase plane wraps more tightly in a given time.

7.1 Set up

The simulations' axisymmetric initial conditions were assigned by the technique of Springel et al. (2005) as implemented in the DICE code (Perret et al. 2014). This technique imposes $\sigma_R = \sigma_z$ and in parts of the disc σ_R fell below the value that makes Toomre (1964)'s stability parameter

$$Q_\star \equiv \frac{\sigma_R \kappa}{3.36 \, G \, \Sigma_\star} = 1.5, \tag{6}$$

where κ and $\Sigma_\star$ are the epicycle frequency and stellar surface density. Where $Q_\star < 1.5$, we increased σ_R (but not σ_ϕ) to ensure $Q_\star \geqslant 1.5$ everywhere. Since the initial conditions are for a system slightly out of equilibrium, each simulation was evolved for roughly 4 Gyr before being disturbed. We refer to the model after this relaxation phase as the 'unperturbed' model (Model P). See Table 1 for details of this model Galaxy,

We disturbed this model in six simulations. The intruders had masses of 1, 5 or 10×10^{10}M$_\odot$ and comprised a 4×10^8M$_\odot$ stellar system embedded in a dark halo. Both the stellar system and the dark halo were truncated Hernquist spheres. Their scale radii were 0.85 and 10 kpc, respectively. The stellar system was truncated at 2.5 kpc while the truncation radius of the dark halo is listed in Table 2. A simulation with each of these masses was started with the intruder at $(R, z) = (21, 45)$ kpc on a hyperbolic orbit of eccentricity $e = 1.3$ and pericentre distance 10 kpc. For each intruder mass, a second simulation was started with the intruder located 125 kpc from the Galactic centre on a 'trefoil' orbit of the type that roughly fits observations of the Sgr dwarf (see Tepper-García & Bland-Hawthorn 2018, and Figure 20). The intruder's tidal radius was set appropriate to a Galactocentric distance of 50 kpc in the case of a hyperbolic orbit and a distance 125 kpc in the case of a trefoil orbit. The simulations with trefoil orbits are labelled K, L and M, while those with hyperbolic orbits are labelled R, S and T. In the most realistic simulation (Model K), the first and second pericentric passages occurred ∼ 2.5 and ∼ 1 Gyr ago, while the last passage occurred 420 Myr ago, consistent with observations (Ibata et al. 1997).
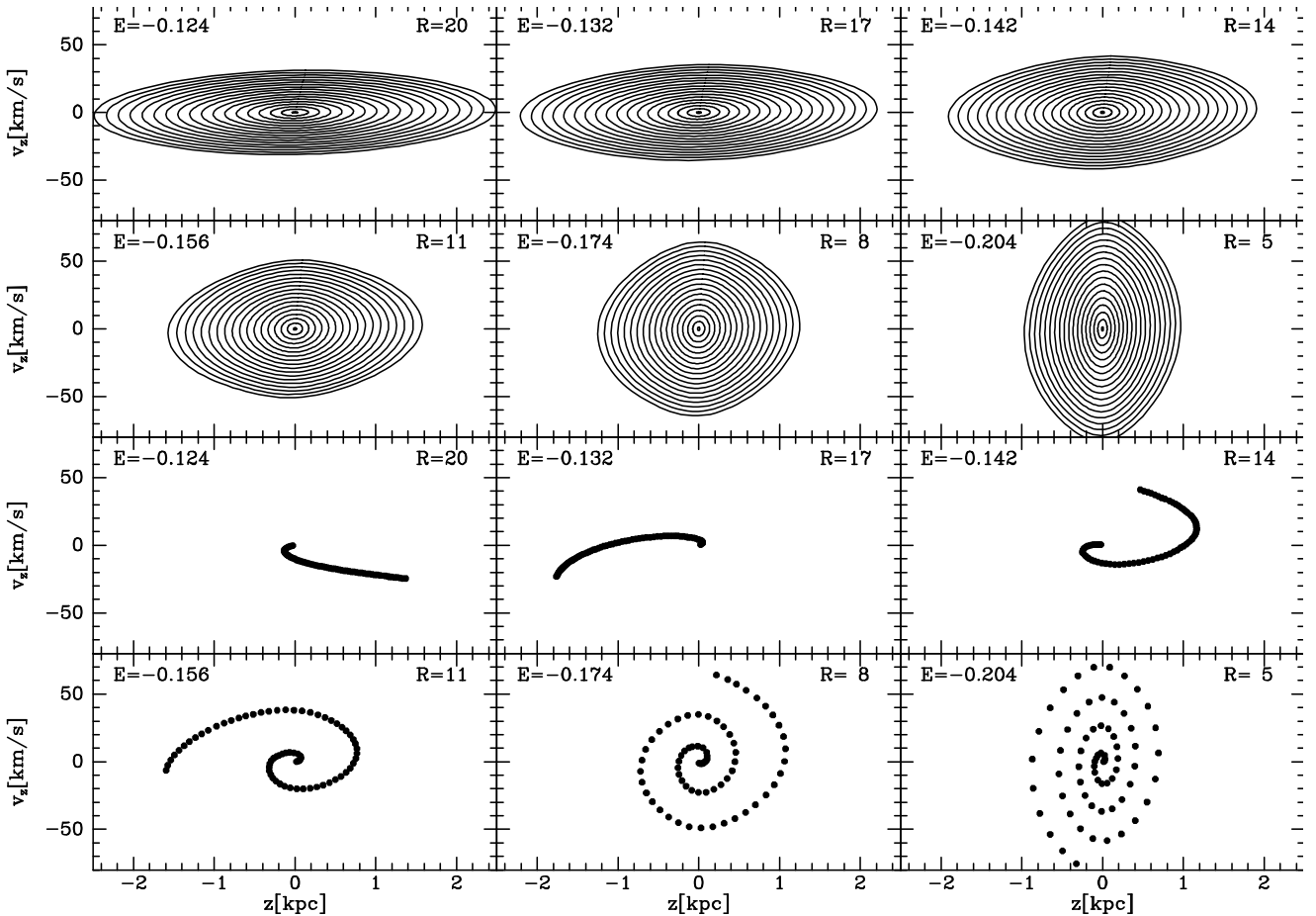
Figure 21. The top 6 panels show surfaces of section in the vertical phase plane (z, V_z) at six different radii (R = 20, 17, 14, 11, 8, 5 kpc) which are chosen to match the radial extent of our new disc simulations and the *Gaia*/GALAH study. The panels were computed with the `AGAMA` software package (Vasiliev 2018) adopting the 'best' Galactic potential from McMillan (2011). Our work is motivated by Antoja's phase spiral pattern at R = 8 kpc: (a) we show only $V_\phi > 0$; (b) the amplitude of the outer ellipse at R = 8 kpc is chosen to match the *Gaia* data; (c) all outermost ellipses in the other panels conserve the same area (= $2\pi J_z$). For each panel, the orbital energies E are indicated. The J_z values for each concentric ellipse moving outwards are: 0.008, 0.20, 0.65, 1.35, 2.31, 3.52, 4.99, 6.71, 8.69, 10.93, 13.42, 16.17, 19.17, 22.43, 25.94, 29.71, 33.73, 38.01 kpc km s^{-1}. In the outer disc, the ellipses elongate in z because stars travel farther and slower in the weaker disc potential. All orbits have radial action $J_R = 0.01$ kpc^2 Myr^{-1} = 9.78 kpc km s^{-1} and J_ϕ for the circular orbit at the quoted radius. The bottom 6 panels coincide with the panels above indicated by the total energies; these reveal the impact of phase wrapping after 250 Myr where all points are initially lined up along $\psi_{\rm ps}$ = 1.3 rad. Across the inner disc, the stronger disc gravity leads to faster vertical oscillations which result in stronger phase wrapping.

7.2 Hyperbolic encounters

In simulations R, S and T with an intruder on a hyperbolic orbit, at $t \sim 95$ Myr the disc moves up towards the approaching intruder and its centre of mass experiences a recoil. Figure 22 and Figure 23 show, for the high- and intermediate-mass intruders respectively, the disc in real space (panels a and b) and in the zV_z phase plane (lower panels) at this time. Numerous signs of disequilibrium are evident in all panels of both figures. In the top panels, we see clear $m = 1$ asymmetry, including a couple of distinct spiral arms, and variations in $\langle V_\phi \rangle$ that have much larger amplitude than those found in the unperturbed simulation P1. These variations seem to be associated wih corrugation waves moving through the disc. In the middle, phase-plane, panels, wisps can be identified that might be part of phase spirals. It is remarkable that there are such features since these figures include particles irrespective of their azimuth or Galactocentric radius, and it

is to be expected that different patterns at widely differing azimuths and radii would wash each other out more completely than they do. Plots that are restricted in radius and azimuth lack the resolution required to trace the spiral.

By $t \sim 130$ Myr, as the intruder crosses the plane at $R \sim 13$ kpc, the entire disc has been shaken. By $t \sim 180$ Myr, the interaction has generated a spiral arm and a strong warp in the outer disc that precesses around the disc (cf. Gómez et al. 2015). The disc does not begin to fall back down towards the receding intruder until after $t = 400$ Myr. The disc is strongly forced by the intruder's tidal field for only ~ 100 Myr but its response persists for the 2 Gyr duration of the simulation.

7.3 Realistic orbit

Contemporary models agree that Sgr initially crossed the disc along a trajectory perpendicular to the Galactic plane ($i \sim 90°$) (e.g. Law et al. 2005; Purcell et al. 2011), but at late

times, as the orbit became circularised by dynamical friction (e.g. Jiang & Binney 2000), the trajectory evolved to one that makes a smaller angle with the disc ($i \lesssim 30°$). As a result of both this change in inclination and the shrinking of the orbit's semi-major axis, passages through the disc became steadily less impulsive. The most recent passage occurred at a radius of about $R \approx 13\,\mathrm{kpc}$.

The lefthand panels of Figure 24 show for Model K the real-space (top two panels) and the phase plane (bottom panel) at $t = 1.77\,\mathrm{Gyr}$, which is $30\,\mathrm{Myr}$ before the high-mass intruder crossed the plane. The righthand panels show the same regions $90\,\mathrm{Myr}$ after the transit. In the bottom left panel showing the phase plane prior to the passage, a phase spiral can be discerned that has vanished from the bottom right panel for the moment after the passage. Closer examination of the data plotted in the bottom left panel of Figure 24 reveals three distinct phase spiral patterns arising in three radial bins ($R = 17, 15, 12\,\mathrm{kpc}$) and their axis ratios vary in line with the predictions of Figure 21. The movie K3 shows that a spiral re-appears as the simulation progresses, so our simulations are consistent with the observed spiral being generated $\sim 400\,\mathrm{Myr}$ ago as Antoja et al. (2018) and Binney & Schönrich (2018) suggested.

We can gain insight into the total (rather than stellar) mass of the Sgr dwarf by combining the simulations with *Gaia* DR2. The low-mass intruder on a realistic orbit (Model M) barely ruffles the disc. The high-mass intruder (Model K), by contrast, produces features with $|z_{\mathrm{max}}| \lesssim 5\,\mathrm{kpc}$ and $|V_{z_{\mathrm{max}}}| \lesssim 50\,\mathrm{km\,s^{-1}}$ that exceed the scale of the *Gaia* features. The intermediate-mass intruder produces disequilibria of about the required amplitude at $R = R_0$. This is consistent with the finding of Binney & Schönrich (2018), who generated a realistic spiral with an intruder of mass $2 \times 10^{10}\,\mathrm{M_\odot}$.

8 CONCLUSIONS

We have used the data from the second releases of the *Gaia* and GALAH surveys to examine the Galactic discs in a sphere of radius $\sim 1\,\mathrm{kpc}$ around the Sun. The GALAH survey allows us to divide the disc into its two fundamental components, the α-rich and the α-poor discs. Traditionally these have been called the thick and thin discs but it is now clear that this terminology can be confusing.

The α-rich disc is old and largely confined to within R_0. We have shown that its velocity-dispersion tensor has a bias towards V_z that is unique in the Galaxy. Although the α-rich disc must have formed rather quickly (and before the α-poor disc started to form), it has a complex internal structure, with its more metal-poor stars being on highly eccentric, low-angular-momentum orbits.

The α-poor disc is the accumulation of up to 10 Gyr of gradually declining star formation. Its history has bequeathed it a complex internal structure that differs from that of the α-rich disc in two key respects: (i) stars with less angular momentum tend to be more rather than less metal-rich; (ii) its stars have larger rather than smaller in-plane velocity dispersions than the dispersion perpendicular to the plane.

Following the discovery by Antoja et al. (2018) of a spiral when $\langle V_\phi \rangle$ is plotted in the zV_z phase plane, we have used *Gaia* and GALAH to examine this plane closely. In this

plane, stars move on ovals whose area is proportional to the vertical action J_z. Hence α-rich stars are widely dispersed in the zV_z plane whereas α-poor stars become less widely dispersed as [Fe/H] decreases. On account of asymmetric drift, $\langle V_\phi \rangle$ decreases as one moves away from the centre of the zV_z plane. On top of this systematic decrease, a spiral is evident in $\langle V_\phi \rangle$ that can be fitted with remarkable accuracy by a Archimedean spiral. Whereas Antoja et al. (2018) extracted the spiral from *Gaia* data for stars that lie in thin cylindrical shell around the Sun, we find that a spiral remains prominent and remarkably invariant when this volume is greatly enlarged and shifted in radius or in azimuth. These findings suggest that the spiral is a global feature of the disc.

Small changes in the structure of the spiral are evident when the data are sliced by the values of actions. The spiral is clearest in stars with less than the median value of J_r. It is somewhat tighter in stars with smaller L_z as one expects from the tendency of the frequency Ω_z of motion in the zV_z plane to increase as L_z decreases.

The spiral is hard to discern in the plot for α-rich stars, in part because the sample of these stars is relatively small. Among the α-poor stars, there is no evidence for variation in the spiral's form or amplitude with [Fe/H]. We show that the spiral can be seen in LAMOST data, but these data do not allow detailed study because they are noisy and the latest data release does not include [α/Fe].

When angle-action coordinates are used to plot the zV_z phase plane, a spiral is evident that coincides well with the curve formed after $515\,\mathrm{Myr}$ by points that start from a common value of the angle variable θ_z. This suggests that the spiral is a relic of a disturbance the disc experienced about 0.5 Gyr ago, in line with the numerical simulations.

A plot of $\langle V_R \rangle$ for *Gaia* DR2 proves to be a superposition of two features: a spiral that is very similar to that seen in the plot for V_ϕ superposed on a quadrupole pattern that we have traced to the morphology of orbits in the Rz meridional plane and the well known tilting of the velocity ellipsoid as one moves away from the plane. The results summarised here establish that the spiral is not associated with the dispersal of stars from theit natal location but, like the structure *Hipparcos* revealed in the UV plane, has arisen through some dynamical process disturbing the Galaxy's equilibrium.

A strong case has been made by Antoja et al. (2018) and Binney & Schönrich (2018) that the spiral is a consequence of the tidal pull of the Galaxy by a halo substructure, possibly the Sgr dwarf, as it crossed the plane $\sim 0.5\,\mathrm{Gyr}$ ago. Binney & Schönrich (2018) simulated this process using two undesirable approximations: that the event was impulsive and that it does not modify the Galaxy's gravitational field. Currently these approximations can only be lifted by doing a full N-body simulation of the event.

In Section 7, we showed results from six such simulations. Even with three million particles, we did not achieve sufficient resolution in the volume for which we have data to construct useful phase planes for this volume. Instead, we have populated the zV_z plane with all stars in a simulation, thus effectively superposing phase planes at all azimuths and many different radii. Remarkably, in light of this superposition, for intruders of mass $5 \times 10^{10}\,\mathrm{M_\odot}$ and above, arms that are consistent with being phase spirals can still be identified in the simulated phase plane. These structures lie outside

R_0, and reach to greater distances from the plane and larger values of $|v_z|$ than the observed spiral.

An intruder of mass $10^{10} M_\odot$ does not perturb the disc enough to generate measurable phase-plane structure, so we tentatively conclude that the observed structure was generated by a body of greater mass. This conclusion is consistent with the finding of Binney & Schönrich (2018).

Natural directions for future work include using the distributions of α-rich and α-poor stars in action-space shown in Figure 4 to build Extended Distribution Functions for the discs (Sanders & Binney 2015), and use these EDFs to construct a self-consistent model Galaxy. Such a model would predict the density and kinematics of the two discs throughout the Galaxy, and thus provide a link to other spectroscopic surveys that can separate the discs at other locations. While the Galaxy is not in equilibrium, the work of Binney & Schönrich (2018) shows the value of such models as frameworks within which to model non-equilibrium features such as the phase spiral.

The wealth of evidence that we now have, that the disc near us is vertically excited, and the strong suspicion that the Sgr dwarf (which was discovered 30 years after the H I warp!) is the prime cause of this excitation, suggests that it is time to develop definitive models of both the warp and the dwarf's orbit. It seems likely that this will be achieved through meticulous and innovative N-body modelling. If satisfactory models can be achieved, they must surely provide conclusive evidence that dark matter, which is dominant in the regions of interest, absorbs energy and momentum from moving massive bodies like ordinary matter. Then we would have conclusive evidence that dark matter comprises non-degenerate fermions rather than being an artifact introduced by using the wrong theory of gravity (Milgrom & Sanders 2008) or being a bosonic condensate of an ultra-light quantum field (Hui et al. 2017, and references therein).

REFERENCES

Adibekyan V. Z., Sousa S. G., Santos N. C., Delgado Mena E., González Hernández J. I., Israelian G., Mayor M., Khachatryan G., 2012, A&A, 545, A32
Antoja T., et al., 2018, preprint, (arXiv:1804.10196)
Aumer M., Binney J., Schönrich R., 2016, MNRAS, 462, 1697
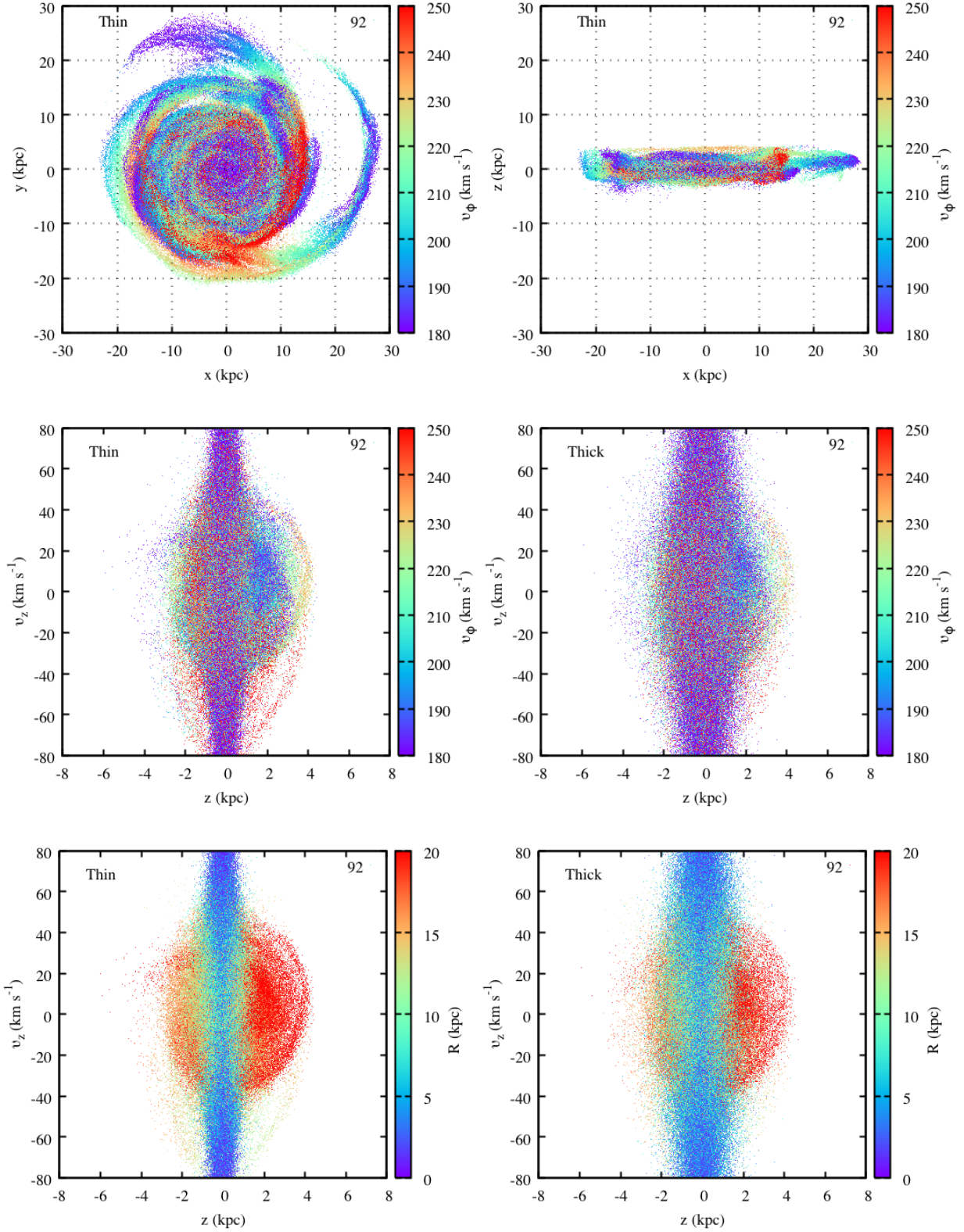
Figure 22. Simulated results for the high mass intruder (Model R; footnote 5) on a hyperbolic orbit where only the Galaxy is shown. (a) *x-y* plane for the thin disc where the particles are colour coded with V_ϕ (Movie R2). (b) *x-z* plane for the thin disc where the particles are colour coded with V_ϕ (Movie R2). (c) $z - V_z$ vertical phase plane for the thin disc colour coded with V_ϕ (Movie R3). (d) $z - V_z$ vertical phase plane for the thick disc colour coded with V_ϕ (Movie R3). (e) $z - V_z$ vertical phase plane for the thin disc colour coded with R (Movie R4). (f) $z - V_z$ vertical phase plane for the thick disc colour coded with R (Movie R4). Note the coherent V_ϕ velocity structures, especially in configuration space and their interrelation across all phase planes, mostly due to strong V_z and weaker V_R motions. The thick disc shows the same extent and structure as the thin disc if one allows for order of magnitude fewer particles. In the vertical phase plane $V_\phi(z, V_z)$ in (c) and (e), there are coherent one-armed phase structures occurring at the same time ($t = 92$ Myr) near 20 kpc (red) and 10 kpc (green).
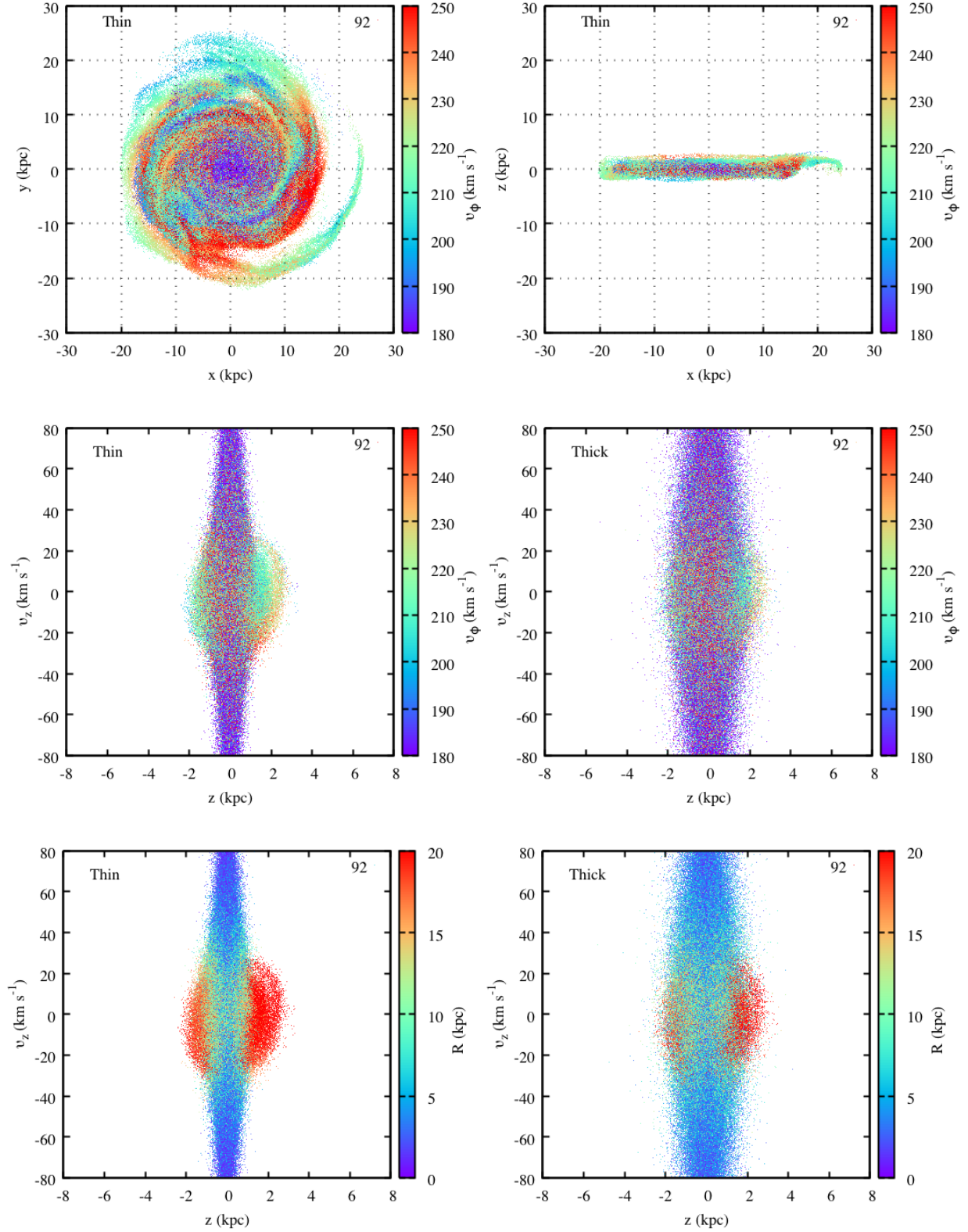
Figure 23. Simulated results for the intermediate mass intruder (Model S; footnote 5) on a hyperbolic orbit where only the Galaxy is shown. (a) *x-y* plane for the thin disc where the particles are colour coded with V_ϕ (Movie S2). (b) *x-z* plane for the thin disc where the particles are colour coded with V_ϕ (Movie S2). (c) $z - V_z$ vertical phase plane for the thin disc colour coded with V_ϕ (Movie S3). (d) $z - V_z$ vertical phase plane for the thick disc colour coded with V_ϕ (Movie S3). (e) $z - V_z$ vertical phase plane for the thin disc colour coded with R (Movie S4). (f) $z - V_z$ vertical phase plane for the thick disc colour coded with R (Movie S4). Once again, there are coherent velocity structures across all phase planes ($t = 92$ Myr). Now the physical and kinematic extent have both declined by almost a factor of two, consistent with the lower intruder mass. In (e), the one-armed phase spiral at 20 kpc is still apparent. The inner phase spiral pattern at $R = 10$ kpc is no longer visible.
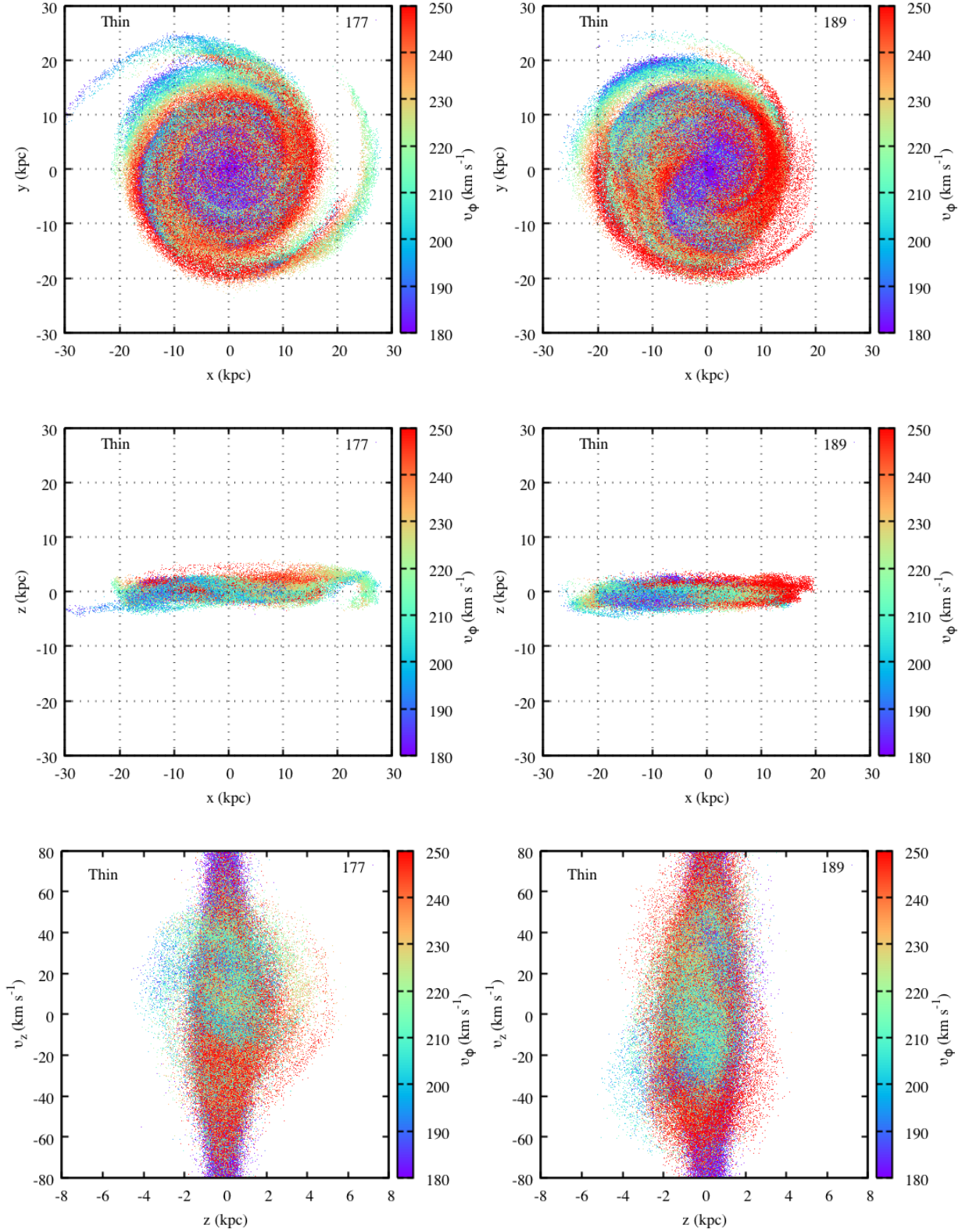
Figure 24. Simulated results for the high mass intruder (Model K; footnote 5) on a realistic Sgr orbit where only the Galaxy is shown. We present results for just before and just after the last disc transit which occurred at 1.8 Gyr in the simulation. (a) *x-y* plane for the thin disc 30 Myr *before* transit where the particles are colour coded with V_ϕ. (b) same as in (a) but 90 Myr *after* the disc crossing. (c) *x-z* plane for the thin disc 30 Myr *before* transit where the particles are colour coded with V_ϕ. (d) same as in (c) but 90 Myr *after* the disc crossing. (e) $z - V_z$ plane 30 Myr *before* the disc crossing. (f) same as (e) but 90 Myr *after* the disc crossing. Note how the coherent phase space structures in (e) are wiped out in (f); the extent in z is also compressed right after the disc transit such that the pattern must rebuild from scratch. Weaker related one-armed structures are seen in $V_R(z, V_z)$ as we observe in the accompanying simulations (Movie K5; footnote 5).

Barden S. C., et al., 2010, in Ground-based and Airborne Instrumentation for Astronomy III. p. 773509, doi:10.1117/12.856103
Binney J., 2012, MNRAS, 426, 1328
Binney J., 2016, MNRAS, 462, 2792
Binney J., Schönrich R., 2018, preprint, (arXiv:1807.09819)
Binney J., Tremaine S., 2008, Galactic Dynamics: Second Edition. Princeton University Press
Binney J., et al., 2014, MNRAS, 439, 1231
Bland-Hawthorn J., Gerhard O., 2016, ARA&A, 54, 529
Bland-Hawthorn J., Kos J., Betters C. H., De Silva G., O'Byrne J., Patterson R., Leon-Saval S. G., 2017, Optics Express, 25, 15614
Brown A. G. A., Vallenari A., Prusti T., de Bruijne J. H. J., Babusiaux C., Bailer-Jones C. A. L., 2018, preprint, (arXiv:1804.09365)
Buder S., et al., 2018, preprint, (arXiv:1804.06041)
Candlish G. N., Smith R., Fellhauer M., Gibson B. K., Kroupa P., Assmann P., 2014, MNRAS, 437, 3702
De Silva G. M., et al., 2015, MNRAS, 449, 2604
Dehnen W., 1998, AJ, 115, 2384
Deng L.-C., et al., 2012, Research in Astronomy and Astrophysics, 12, 735
Eyer L., et al., 2018, preprint, (arXiv:1804.09382)
Famaey B., Jorissen A., Luri X., Mayor M., Udry S., Dejonghe H., Turon C., 2005, A&A, 430, 165
Fouvry J. B., Pichon C., Magorrian J., Chavanis P. H., 2015, A&A, 584, A129
Fouvry J.-B., Pichon C., Chavanis P.-H., Monk L., 2017, MNRAS, 471, 2642
Freeman K., Bland-Hawthorn J., 2002, ARA&A, 40, 487
Freeman K., Bland-Hawthorn J., 2008, in Kodama T., Yamada T., Aoki K., eds, Astronomical Society of the Pacific Conference Series Vol. 399, Panoramic Views of Galaxy Formation and Evolution. p. 439
Gilmore G., Reid N., 1983, MNRAS, 202, 1025
Goldreich P., Lynden-Bell D., 1965, MNRAS, 130, 125
Gómez F. A., Besla G., Carpintero D. D., Villalobos Á., O'Shea B. W., Bell E. F., 2015, ApJ, 802, 128
Gravity Collaboration et al., 2018, A&A, 615, L15
Hayden M. R., et al., 2015, ApJ, 808, 132
Hernquist L., 1990, ApJ, 356, 359
Holmberg J., Nordström B., Andersen J., 2009, A&A, 501, 941
Hui L., Ostriker J. P., Tremaine S., Witten E., 2017, Phys. Rev. D, 95, 043541
Hunter C., Toomre A., 1969, ApJ, 155, 747
Ibata R. A., Wyse R. F. G., Gilmore G., Irwin M. J., Suntzeff N. B., 1997, AJ, 113, 634
Ida S., Kokubo E., Makino J., 1993, MNRAS, 263, 875
Jenkins A., Binney J., 1990, MNRAS, 245, 305
Jiang I.-G., Binney J., 2000, MNRAS, 314, 468
Jordi C., et al., 2010, A&A, 523, A48
Koppelman H. H., Helmi A., Veljanoski J., 2018, preprint, (arXiv:1804.11347)
Kos J., et al., 2017, MNRAS, 464, 1259
Kos J., et al., 2018b, preprint, (arXiv:1804.05851)
Kos J., et al., 2018a, preprint, (arXiv:1807.00822)
Law D. R., Johnston K. V., Majewski S. R., 2005, ApJ, 619, 807
Lynden-Bell D., 1967, MNRAS, 136, 101
Malhan K., Ibata R. A., Martin N. F., 2018, preprint, (arXiv:1804.11339)
Marchetti T., Rossi E. M., Brown A. G. A., 2018, preprint, (arXiv:1804.10607)
Martell S. L., et al., 2017, MNRAS, 465, 3203
McMillan P. J., 2011, MNRAS, 414, 2446
McMillan P. J., 2017, MNRAS, 465, 76
Milgrom M., Sanders R. H., 2008, ApJ, 678, 131
Miyamoto M., Nagai R., 1975, PASJ, 27, 533

Nordström B., et al., 2004, A&A, 418, 989
Perret V., Renaud F., Epinat B., Amram P., Bournaud F., Contini T., Teyssier R., Lambert J.-C., 2014, A&A, 562, A1
Perryman M. A. C., et al., 2001, A&A, 369, 339
Prusti T., et al., 2016, A&A, 595, A1
Purcell C. W., Bullock J. S., Tollerud E. J., Rocha M., Chakrabarti S., 2011, Nature, 477, 301
Reid M. J., Brunthaler A., 2004, ApJ, 616, 872
Sanders J. L., Binney J., 2015, MNRAS, 449, 3479
Schönrich R., 2012, MNRAS, 427, 274
Schönrich R., Binney J., 2009, MNRAS, 396, 203
Schönrich R., Dehnen W., 2018, MNRAS, 478, 3809
Sellwood J. A., Binney J. J., 2002, MNRAS, 336, 785
Sellwood J. A., Carlberg R. G., 2014, ApJ, 785, 137
Sharma S., 2017, ARA&A, 55, 213
Sharma S., Bland-Hawthorn J., Johnston K. V., Binney J., 2011, ApJ, 730, 3
Sharma S., et al., 2014, ApJ, 793, 51
Sharma S., et al., 2018, MNRAS, 473, 2004
Sheinis A., et al., 2015, Journal of Astronomical Telescopes, Instruments, and Systems, 1, 035002
Siebert A., et al., 2008, MNRAS, 391, 793
Solway M., Sellwood J. A., Schönrich R., 2012, MNRAS, 422, 1363
Spagna A., Lattanzi M. G., Re Fiorentin P., Smart R. L., 2010, A&A, 510, L4
Springel V., Di Matteo T., Hernquist L., 2005, MNRAS, 361, 776
Tepper-García T., Bland-Hawthorn J., 2018, MNRAS, 478, 5263
Tepper-García T., Bland-Hawthorn J., Binney J., Sharma S., GALAH team 2019, preprint (arXiv:in preparation)
Teyssier R., 2002, A&A, 385, 337
Toomre A., 1964, ApJ, 139, 1217
Toomre A., 1969, ApJ, 158, 899
Toomre A., 1981, in Fall S. M., Lynden-Bell D., eds, Structure and Evolution of Normal Galaxies. pp 111–136
Vasiliev E., 2018, AGAMA: Action-based galaxy modeling framework, Astrophysics Source Code Library (ascl:1805.008)
Wittenmyer R. A., et al., 2018, AJ, 155, 84
Xu Y., Newberg H. J., Carlin J. L., Liu C., Deng L., Li J., Schönrich R., Yanny B., 2015, ApJ, 801, 105
Zwitter T., et al., 2018, preprint, (arXiv:1804.06344)

APPENDIX A: MOVIES

A1 Reference model: isolated Galaxy

In movie P1,[5] we witness the long-term evolution of the isolated Galaxy model (Model P) summarised in Table 1. The frames are shown with time steps of $\Delta t = 10$ Myr which is short enough to trace most stellar orbits reliably. The disc settles to an equilibrium configuration within a few hundred Myr. This can be seen from the settling to a cold, thin disc in the edge-on and face-on projections, with a constant vertical scaleheight. The disc generates low-level flocculent spiral perturbations consistent with the intrinsic numerical and spatial resolution, but individual stellar orbits confirm that the coarse-grained potential is well behaved. The simulation includes a thick disc which is shown only in the vertical phase plane. Since the thick disc is older and more metal poor than the thin disc, including two discs allows us to study the predicted age and metallicity dependence of the

---

[5] http://www.physics.usyd.edu.au/~tepper/proj_galah_paper.html

cohent spiral. This is the base model we use to study the perturbation induced by an intruder.

In movie P2, we show the same configuration space for movie P1, but now each star is colour-coded by its azimuthal velocity V_ϕ in the plane of the disc. The velocity field reflects the underlying rotation curve consistent with the total gravitational potential. This becomes relevant when comparing to the perturbed cases below. There are small variations across the disc consistent with the stochastic spiral perturbations.

In movie P3, we show the evolution of the thin and thick discs in the vertical phase plane (z, V_z) coded by the azimuthal velocity V_ϕ, i.e. $V_\phi(z, V_z)$. There is no statistical averaging $\langle V_\phi \rangle$ over the population as carried out for the *Gaia* data (e.g. Figure 5). These are projections of the *entire* disc population and so are dominated by the inner disc with its higher V_z motions compressed in z. The different vertical thicknesses are evident and they remain fairly constant as the disc evolves. Each star moves clockwise around $(z, V_z) = (0,0)$ as it oscillates in the disc potential with an angular frequency Ω_z. No coherent patterns emerge because the phases are randomised over 2π.

A2   Perturbed model: hyperbolic orbit

Movies S1 and R1 show the interaction of the Galaxy with the intermediate-mass and high-mass intruders respectively, each on the hyperbolic orbit (shown as a filled red circle) crossing the disc at about $R = 13$ kpc. At $t \sim 95$ Myr the disc move up towards the approaching intruder and its centre of mass experiences a recoil. By the time the intruder has transited the disc plane, the entire disc has responded to the perturber. By $t = 180$ Myr, the interaction has excited a spiral arm and a strong warp in the outer disc that precesses in the plane around the centre of mass (cf. Gómez et al. 2015). The upwards momentum of the disc does not reverse until after $t = 400$ Myr. The strong forcing by the perturber is active for less than 100 Myr but the disc response persists for the 2 Gyr duration of the movie. For reference, the results are also shown in Figure 22 and Figure 23 respectively at a single timestep ($t = 900$ Myr).

In Figure 22 (R2) and Figure 23 (S2), when compared to the isolated Galaxy model (movie P2), the azimuthal velocity field V_ϕ shows systematic variations due to the low-amplitude bending waves (corrugations or wrinkles) propagating through the disc. The kinematically distinct, azimuthal 'plumes' (confined in radius) arise from disc segments displaced vertically by varying amounts, with larger displacements resulting in bigger lags with respect to the disc rotation at that radius. In other words, these kinematic plumes are mostly associated with large V_z motion and some V_R motion.

In Figure 22 (R3) and Figure 23 (S3), these same kinematic plumes encoded with the same V_ϕ velocities manifest in the (z, V_z) plane. For example, we show plumes at two different radii for a single timestep ($t = 900$ Myr). In R3, the spiral feature at 10 kpc aligns and elongates with the disc whereas the feature in the outer disc appears more circular as expected from theory (Figure 21).

At times, a one-armed spiral feature is clear (e.g. movies S3 and R3 during $1.2 < t < 1.9$ Gyr) although tracing it to the origin in (z, V_z) proves to be difficult without the action analysis (Section 4.3) applied directly to the models

(Tepper-García et al. 2019). This is because our sampling (limited by N_P) is not sufficient to provide contrast against the clockwise population from the dominant underlying disc. In the absence of another disc-transiting event, these spiral features can be long-lived ($\gtrsim 500$ Myr) in the vertical phase plane.

In Figure 22, for the high-mass intruder (R3), there are several coherent one-armed plumes in the (z, V_z) plane. Once again, these grow to their maximum amplitude in $|z_{max}| \approx 6$ kpc and $|V_{z_{max}}| \approx 60$ km s^{-1} long after the transit has occurred. This appears to be associated with the strong vertical recoil of the disc after its reversal along the intruder's orbit. In particular, note the coherent *elliptic* plume aligned with and encircling the disc ($V_z < 0$) emerging at $t = 900$ Myr and persisting for 100 Myr. The low value of $\mathcal{A}_z$ (Figure 21) reinforces that this feature occurs at smaller radius ($R \approx 13 - 15$ kpc). There are spiral plumes down to maybe $R \approx 10$ kpc but insufficiently populated to give good contrast. This is a failing of the current models. Much larger simulations with an order of magnitude more particles are already under way.

In Figure 23, for the intermediate-mass intruder (S3), we see the kinematic spiral has lower amplitude in both axes. It grows out of the disc, rotates as a fixed pattern, reaching its maximum amplitude in $|z_{max}| \approx$ 2.5-3 kpc and $|V_{z_{max}}| \approx 30 - 40$ km s^{-1}. In Figure 23 (S4), the vertical phase plane is encoded with the Galactocentric radius R: we see that the coherent spiral patterns occur at $R \approx 15 - 20$ kpc. (These features may also be associated with the reversal of the disc's momentum parallel to the intruder's orbit.) We note that $|z_{max}|$ and $|V_{z_{max}}|$ approximately match the predicted values in Figure 21 at $R = 20$ kpc; the model effectively "calibrates" the expected amplitudes at other radii, in particular the anticipated values of $|z_{max}| \approx 1$ kpc and $|V_{z_{max}}| \approx 50$ km s^{-1} at $R \approx R_0$ (Antoja et al. 2018). We see the effects of the phase spiral at lower radii down to 10 kpc but the contrast is poor.

In Figure 22 (R4), the strongest phase spiral signal is further out at $R \approx 20$ kpc. The outer disc of the Galaxy must be experiencing a strong forced oscillation, with stars confined to well-defined corrugations or wrinkles (Schönrich & Dehnen 2018). This is a strong prediction of our simulations given the low-flying orbit of Sgr over the disc. It seems reasonable to consider that this is the explanation for the TriAndromeda and Monoceros "rings" discovered by the SDSS survey towards the outer stellar disc (Xu et al. 2015) and maybe even most of the wave-like structure, ripples and corrugations claimed to date (Schönrich & Dehnen 2018).

A3   Perturbed model: realistic orbit

In movie M1 (footnote 5), we present our model for the low-mass Sgr impact along a realistic orbit (see Tepper-García & Bland-Hawthorn 2018). Contemporary models agree that Sgr initially crossed the disc along a trajectory perpendicular to the Galactic plane (e.g. Law et al. 2005; Purcell et al. 2011). But at late times, as the orbit became circularised by dynamical friction (e.g. Jiang & Binney 2000), the trajectory evolved to be more inclined to the disc ($i \lesssim 30°$), and therefore less impulsive. The last crossing occurred at a radius of about $R \approx 13$ kpc.

All of the movies from Model M look very similar to the unperturbed case (Model P), with the exception of one.

When we compare model M3 to the stable model P3 for the thin disc, there is clear evidence of heating in the former due to the action of the low-mass perturber. Such dynamical heating can happen over the disc where the forcing frequency is out of phase with the intrinsic disc response. This heating also occurs in the high-mass and intermediate-mass cases but this is obscured by the dramatic plumes arising from the disc.

In movies L and K (footnote 5), we present our model for the intermediate and high mass impacts respectively along essentially the same orbit. In Figure 24, we show frames from movie K4 at two different timesteps, 30 Myr before and 90 Myr after a disc transit. This is to emphasise how clean the phase spiral signature is right before impact, and how it is wiped out for up to $\approx 100 - 150$ Myr after the impact, reforming thereafter.

In Figure 24(e), there are three distinct phase spiral patterns arising in three radial bins ($R = 17, 15, 12$ kpc). We can calibrate the strength of the signal in Antoja et al. (2018) from our numerical simulations, confirmed by the single crossing hyperbolic models. The low-mass intruder (Model M) barely ruffles the disc. The high-mass intruder (Model K) produces features with $|z_{max}| \lesssim 5$ kpc and $|V_{z_{max}}| \lesssim 50$ km s^{-1}, comparable to the results for the high-mass hyperbolic case (Model R). The intermediate-mass case scales down as it did for the hyperbolic models, thus consistent with the amplitude of the Antoja spiral at $R = R_0$. In movie K5, we show the phase spiral pattern also occurs in $V_R(z, V_z)$ for the same features observed in $V_\phi(z, V_z)$, albeit with less contrast.

After impact, the spiral features do arise again from the ashes and are persistent until the next impact. The fact that we see a clear phase spiral today is consistent with the passage of time since the last crossing about 400 Myr ago (by general consensus) and our imminent disc crossing in $\gtrsim 50$ Myr. This makes the spiral phenomenon no older than about 250 Myr.

[1]Sydney Institute for Astronomy, School of Physics, A28, The University of Sydney, NSW 2006, Australia
[2]Center of Excellence for Astrophysics in Three Dimensions (ASTRO-3D), Australia
[3]Miller Professor, Miller Institute, University of California Berkeley, CA 94720, USA
[4]Rudolf Peierls Centre for Theoretical Physics, Clarendon Laboratory, Oxford, OX1 3PU, UK
[5]Research School of Astronomy & Astrophysics, Australian National University, ACT 2611, Australia
[6]Department of Physics and Astronomy, Macquarie University, Sydney, NSW 2109, Australia
[7]Max Planck Institute for Astronomy (MPIA), Koenigstuhl 17, 69117 Heidelberg, Germany
[8]Fellow of the International Max Planck Research School for Astronomy & Cosmic Physics at the University of Heidelberg, Germany
[9]Monash Centre for Astrophysics, Monash University, Australia
[10]School of Physics and Astronomy, Monash University, Australia
[11]INAF Astronomical Observatory of Padova, 36012 Asiago, Italy
[12]ICRAR, The Uni. of Western Australia, 35 Stirling Highway, Crawley, WA 6009, Australia
[13]Department of Physics and Astronomy, Uppsala University, Box 516, SE-751 20 Uppsala, Sweden
[14]School of Physics, UNSW, Sydney, NSW 2052, Australia
[15]Department of Astronomy, Columbia University, Pupin Physics Laboratories, New York, NY 10027, USA
[16]Center for Computational Astrophysics, Flatiron Institute, 162 Fifth Avenue, New York, NY 10010, USA
[17]Faculty of Mathematics and Physics, University of Ljubljana, Jadranska 19, 1000 Ljubljana, Slovenia

This paper has been typeset from a TeX/LaTeX file prepared by the author.